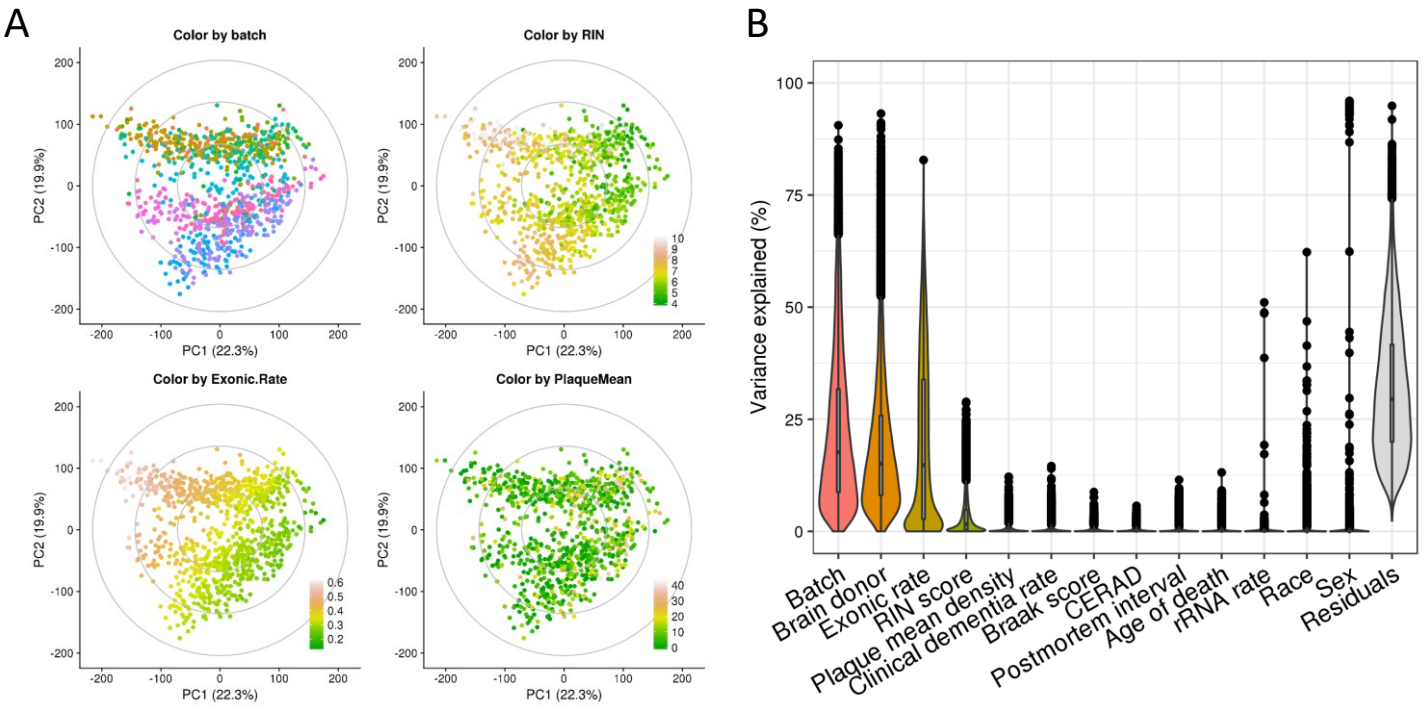

Fig. S1. RNA-seq data correction for confounding factors, related to STAR Methods. A, Principal component (PC) plots showing the association between biological/technical variables and top PCs. **B**, Distribution of variance explained by the biological/technical variables according to variancePartition analysis. From left to right, variables were sorted in descending order by median fraction of variance explained.

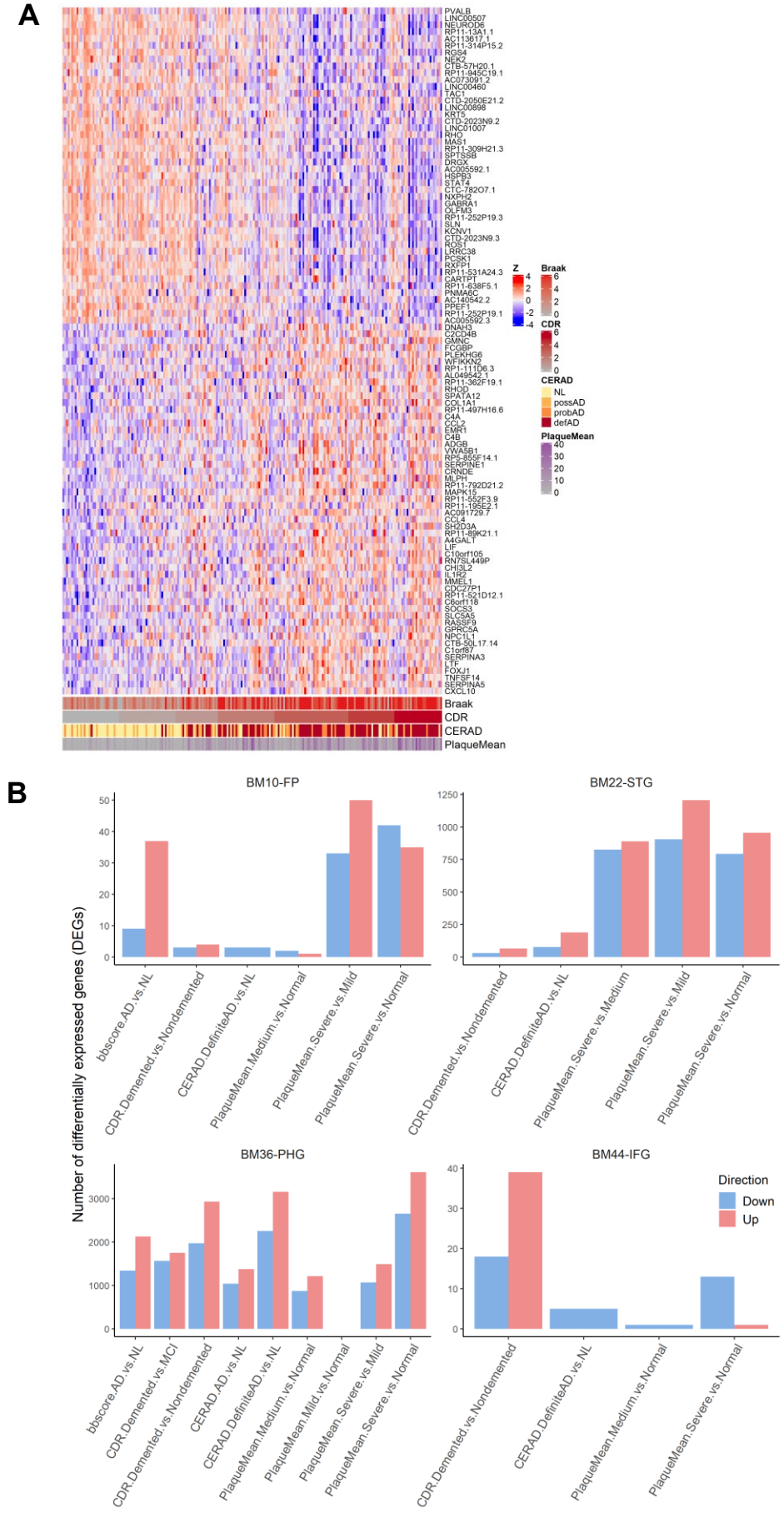

Fig. S2. Summary of differential expression signatures, related to STAR Methods. A, Heat-map showing the expression variation of top 100 differentially expressed genes (DEGs) ranked by fold change in the BM36-PHG region. The expression of each gene were scaled into z-values. Sample-level trait values were annotated in the bottom. **B**, bar-plot showing the number of DEGs identified in each contrast for each region regarding 4 different cognitive/neuropathological traits. X-axis denotes the trait-specific contrast. Down, down-regulated DEGs; Up, up-regulated DEGs.

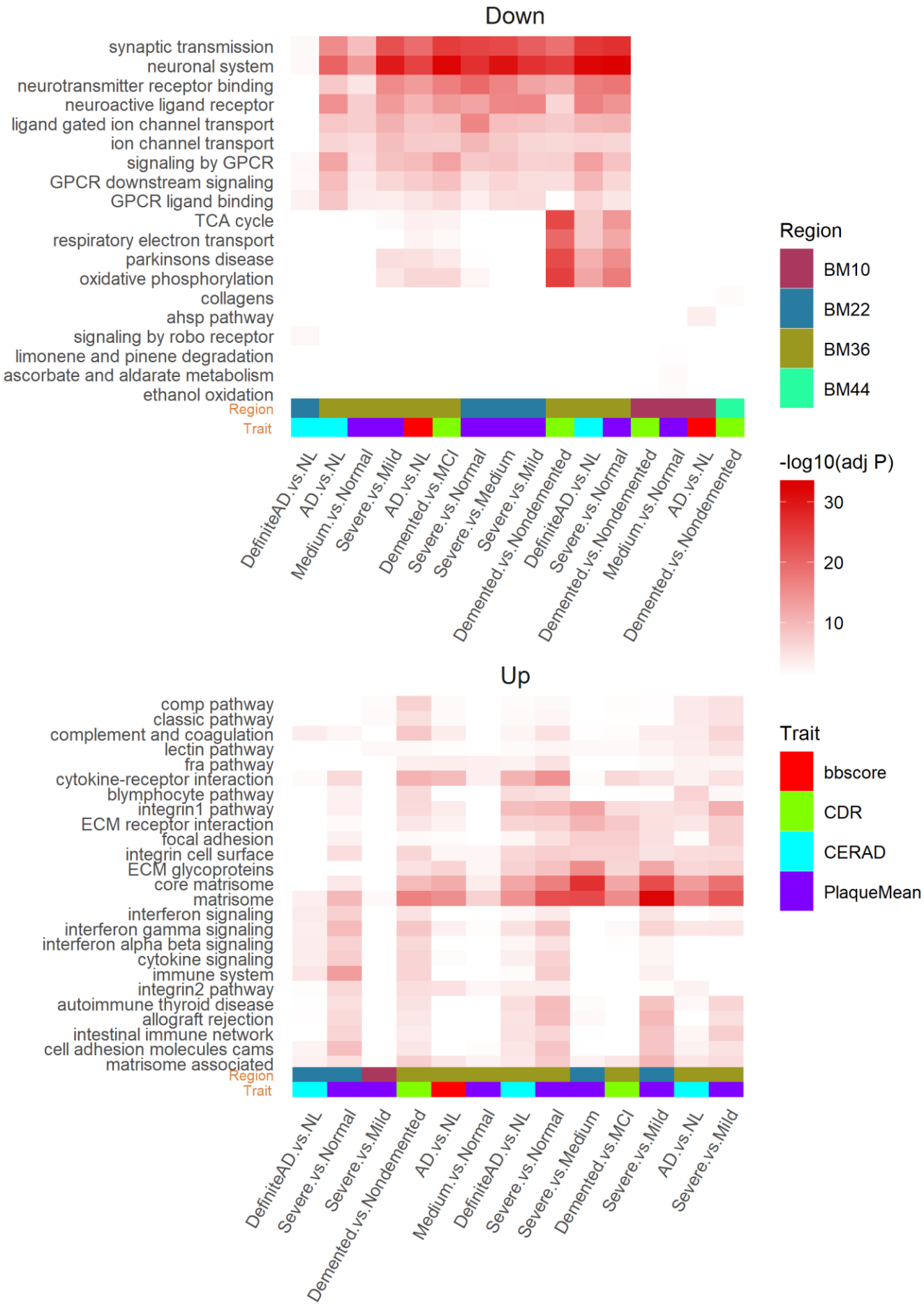

Fig. S3. Summary of gene ontology (GO)/pathways enriched in differential expression signatures, related to STAR Methods. Top pathways enriched in the present down-regulated (top) or up-regulated (bottom) DEGs. Columns denote different set of DEGs from 4 brain regions regarding 4 different cognitive/neuropathological traits and rows denote GO/pathways. Down, down-regulated DEGs; Up, up-regulated DEGs.

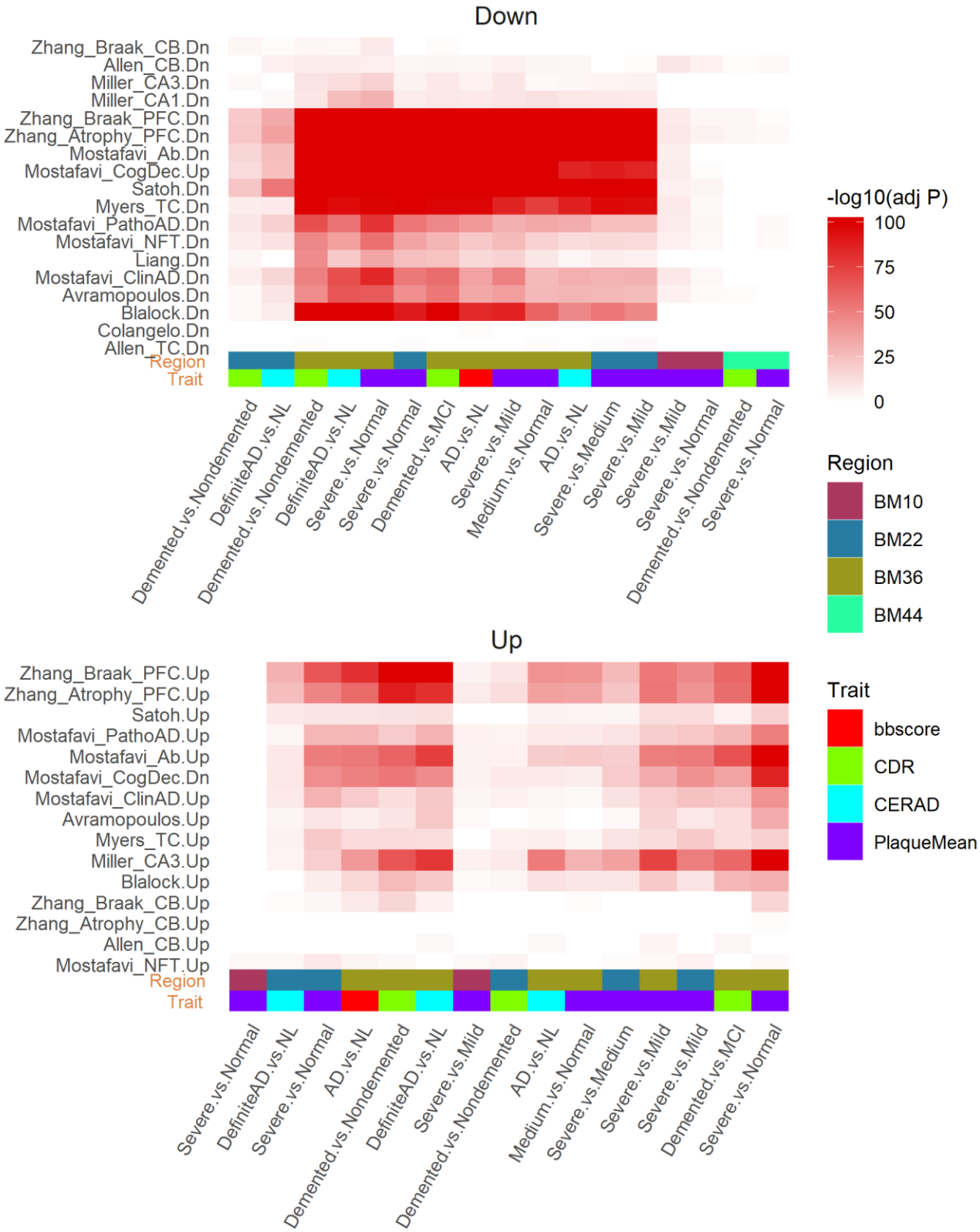
Down
Zhang_Braak_CB.Dn
Allen_CB.Dn
Miller_CA3.Dn
Miller_CA1.Dn
Zhang_Braak_PFC.Dn
Zhang_Atrophy_PFC.Dn
Mostafavi_Ab.Dn
Mostafavi_CogDec.Up
Satoh.Dn
Myers_TC.Dn
Mostafavi_PathoAD.Dn
Mostafavi_NFT.Dn
Liang.Dn
Mostafavi_ClinAD.Dn
Avramopoulos.Dn
Blalock.Dn
Colangelo.Dn
Allen_TC.Dn
Region
Trait
Demented.vs.Nondemented
DefiniteAD.vs.NL
Demented.vs.Nondemented
DefiniteAD.vs.NL
Severe.vs.Normal
Severe.vs.Normal
Demented.vs.MCI
AD.vs.NL
Severe.vs.Mild
Medium.vs.Normal
AD.vs.NL
Severe.vs.Medium
Severe.vs.Mild
Severe.vs.Mild
Severe.vs.Normal
Demented.vs.Nondemented
Severe.vs.Normal
-log10(adj P)
100
75
50
25
0
Region
BM10
BM22
BM36
BM44
Up
Zhang_Braak_PFC.Up
Zhang_Atrophy_PFC.Up
Satoh.Up
Mostafavi_PathoAD.Up
Mostafavi_Ab.Up
Mostafavi_CogDec.Dn
Mostafavi_ClinAD.Up
Avramopoulos.Up
Myers_TC.Up
Miller_CA3.Up
Blalock.Up
Zhang_Braak_CB.Up
Zhang_Atrophy_CB.Up
Allen_CB.Up
Mostafavi_NFT.Up
Region
Trait
Severe.vs.Normal
DefiniteAD.vs.NL
Severe.vs.Normal
AD.vs.NL
Demented.vs.Nondemented
DefiniteAD.vs.NL
Severe.vs.Mild
Demented.vs.Nondemented
AD.vs.NL
Medium.vs.Normal
Severe.vs.Medium
Severe.vs.Mild
Severe.vs.Mild
Demented.vs.MCI
Severe.vs.Normal
Trait
bbscore
CDR
CERAD
PlaqueMean

Fig. S4. Preservation of differential expression signatures in published bulk-tissue transcriptomic analysis datasets, related to STAR Methods. Public AD signatures enriched in the present down-regulated (top) or up-regulated (bottom) DEGs. In each panel, columns denote the present region-specific DEGs stratified by region, trait and contrast. The rows denote public AD signatures written in a format of "signature.direction", where "direction" is either Dn (down-regulated) or Up (up-regulated), and "signature" includes: 1) Allen_CB, signature detected in the cerebellum region from Allen et al 2018, 2) Allen_TC, signature detected in the temporal cortex region from Allen et al 2018, 3) Avramopoulos, signature detected in the temporal lobe from Avramopoulos et al 2011, 4) Blalock, signature detected in the hippocampus from Blalock et al 2004, 5) Colangelo, signature detected in the hippocampus CA1 region from Colangelo et al 2002, 6) Liang, signature detected in multiple cortex areas from Liang et al 2008, 7) Miller_CA1, signature detected in the hippocampus CA1 region from Miller et al 2013, 8) Miller_CA3, signature detected in the hippocampus CA3 region from Miller et al 2013, 9) Mostafavi_Ab, signature correlated with B amyloid in the prefrontal cortex (PFC) region from Mostafavi et al 2018, 10) Mostafavi_ClinAD, signature correlated with clinical diagnostic of AD in the PFC from Mostafavi et al 2018, 11) Mostafavi_CogDec, signature correlated with cognitive decline in the PFC from Mostafavi et al 2018, 12) Mostafavi_PathoAD, signature correlated with AD pathology in the PFC from Mostafavi et al 2018, 13) Satoh; signature detected in the frontal cortex region from Satoh et al 2014, 14) Myers_TC, signature computed by comparing gene expression between AD and control with limma from the temporal cortex region from Webster et al 2009, 15) Zhang_Atrophy_CB, signature correlated with atrophy in the cerebellum region from Zhang et al 2013, 16) Zhang_Atrophy_PFC, signature correlated with atrophy in the PFC from Zhang et al 2013, 17) Zhang_Braak_CB, signature correlated with Braak staging in the cerebellum region from Zhang et al 2013, 18) Zhang_Braak_PFC, signature correlated with Braak staging in the PFC from Zhang et al 2013. The references of the public AD signatures are listed in supplementary text.

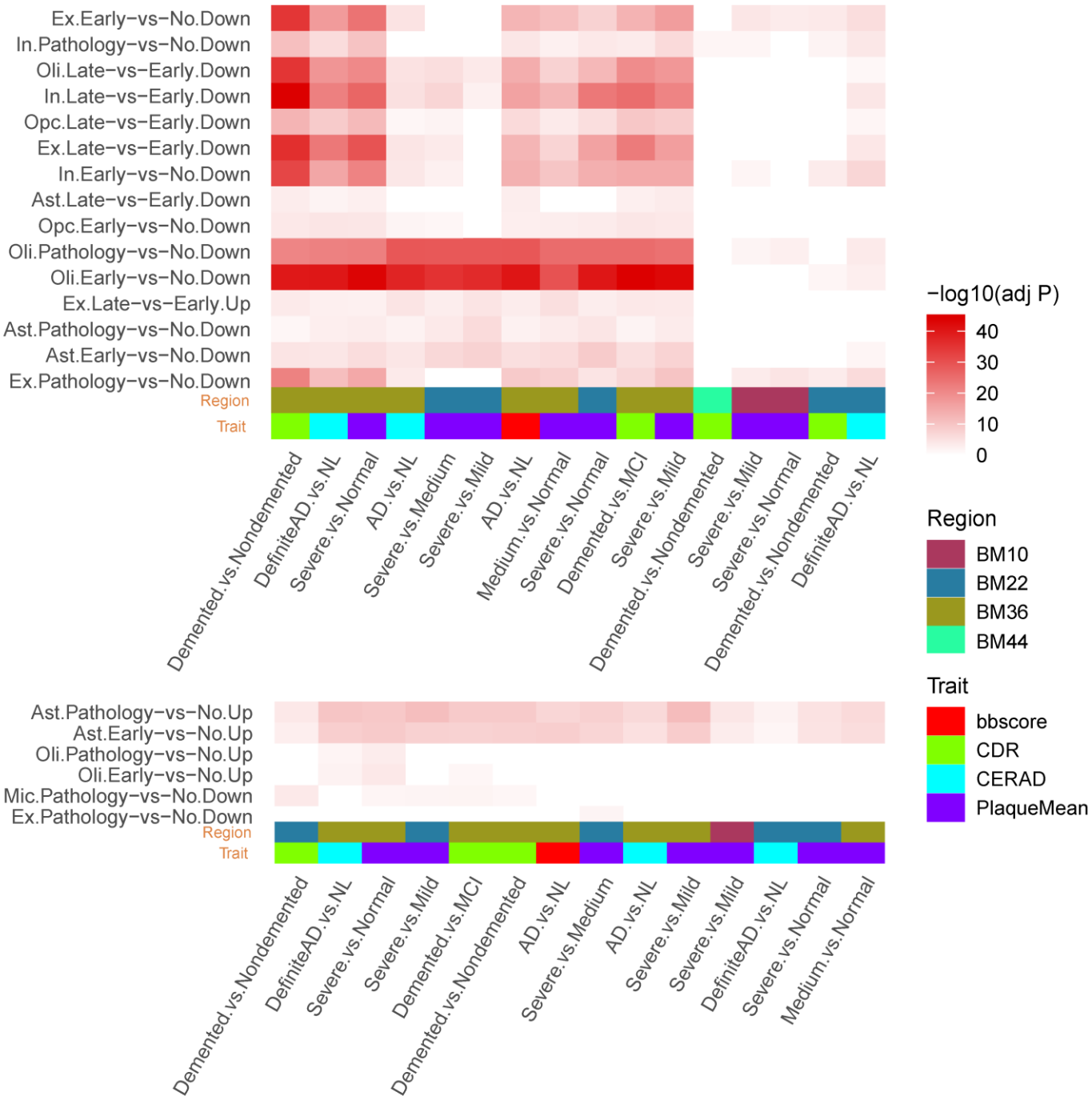

Fig. S5. Preservation of differential expression signatures in a public single-nucleus RNA-seq (snRNA-seq) analysis of AD and control brains, related to STAR Methods. The present down-regulated (top) or up-regulated (bottom) DEGs were enriched in cell type-specific AD signatures detected by snRNA-seq (Mathys et al 2019). Columns denote the present DEG signatures identified from 4 brain regions regarding 4 different cognitive/neuropathological traits and rows denote cell type-specific DEGs. The snRNA-seq cell type-specific DEGs are denoted in a format of "cell.contrast.direction", where cell is either Ex (excitatory neurons), In (inhibitory neurons), Oli (oligodendrocytes), Opc (oligodendrocyte progenitor cells), Ast (astrocytes), or Mic (microglia), contrast is either Early-vs-No (early pathology versus no pathology), Late-vs-Early (late pathology versus early pathology), or Pathology-vs-No (early and late pathology combined versus no pathology), and direction is either Down (down-regulation) or Up (up-regulation).

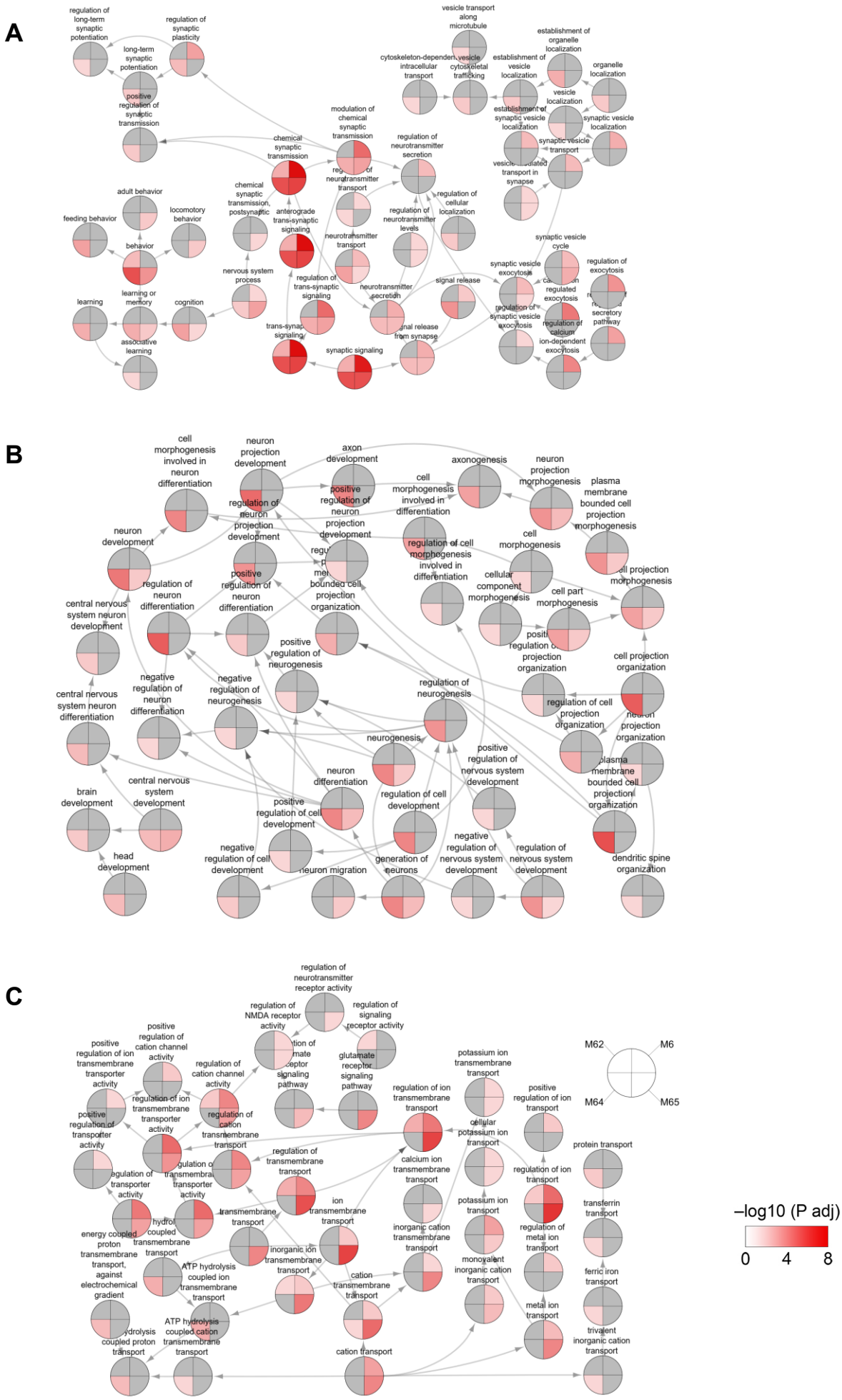
A
regulation of long-term synaptic potentiation
regulation of synaptic plasticity
long-term synaptic potentiation
positive regulation of synaptic transmission
vesicle transport along microtubule
establishment of organelle localization
cytoskeleton-dependent intracellular transport
cytoskeletal trafficking
establishment of vesicle localization
organelle localization
vesicle localization
establishment of synaptic vesicle localization
synaptic vesicle localization
synaptic vesicle transport
modulation of chemical synaptic transmission
chemical synaptic transmission
regulation of neurotransmitter secretion
regulation of neurotransmitter transport
chemical synaptic transmission, postsynaptic
anterograde trans-synaptic signaling
regulation of cellular localization
regulation of neurotransmitter levels
neurotransmitter transport
adult behavior
feeding behavior
locomotory behavior
behavior
nervous system process
regulation of trans-synaptic signaling
neurotransmitter secretion
signal release
synaptic vesicle cycle
synaptic vesicle exocytosis
regulation of exocytosis
regulation of synaptic vesicle exocytosis
regulation of calcium ion-dependent exocytosis
learning
learning or memory
cognition
associative learning
synaptic signaling
B
cell morphogenesis involved in neuron differentiation
neuron projection development
axon development
axonogenesis
neuron projection morphogenesis
plasma membrane bounded cell projection morphogenesis
regulation of neuron projection development
positive regulation of neuron projection development
cell morphogenesis involved in differentiation
neuron development
regulation of cell morphogenesis involved in differentiation
cell morphogenesis
cellular component morphogenesis
cell part morphogenesis
regulation of neuron differentiation
positive regulation of neuron differentiation
central nervous system neuron development
positive regulation of neurogenesis
cell projection organization
negative regulation of neuron differentiation
negative regulation of neurogenesis
regulation of neurogenesis
central nervous system neuron differentiation
neurogenesis
positive regulation of nervous system development
neuron differentiation
regulation of cell development
central nervous system development
brain development
positive regulation of cell development
negative regulation of cell development
generation of neurons
negative regulation of nervous system development
regulation of nervous system development
head development
neuron migration
dendritic spine organization
C
regulation of neurotransmitter receptor activity
regulation of NMDA receptor activity
regulation of signaling receptor activity
glutamate receptor signaling pathway
positive regulation of cation channel activity
positive regulation of ion transmembrane transporter activity
regulation of cation channel activity
regulation of ion transmembrane transporter activity
positive regulation of transporter activity
regulation of cation transmembrane transport
regulation of transmembrane transport
regulation of transporter activity
ion transmembrane transport
transmembrane transport
energy coupled proton transmembrane transport, against electrochemical gradient
hydrol coupled transmembrane transport
inorganic ion transmembrane transport
ATP hydrolysis coupled ion transmembrane transport
cation transmembrane transport
ATP hydrolysis coupled cation transmembrane transport
ydrolysis coupled proton transport
cation transport
potassium ion transmembrane transport
regulation of ion transmembrane transport
positive regulation of ion transport
cellular potassium ion transport
protein transport
calcium ion transmembrane transport
regulation of ion transport
potassium ion transport
transferrin transport
inorganic cation transmembrane transport
regulation of metal ion transport
monovalent inorganic cation transport
ferric iron transport
metal ion transport
trivalent inorganic cation transport
M62
M6
M64
M65
–log10 (P adj)
0
4
8

Fig. S6. GO biological process (BP) hierarchy enrichment reveals distinct functional roles that the top-ranked neuronal/synaptic modules may play, related to Figure 2. Each node denotes a GO/BP term, with a pie-chart displaying the $-\log_{10}$(adjusted P value) of the FET enrichment for the 4 top-ranked neuronal/synaptic modules (i.e. M6, M62, M64 and M65). Arrows denote the direction from a parent term to a child term. The GO hierarchy was extracted from the R/Bioconductor package GO.db and the GO/BP annotation gene sets were obtained from the R/Bioconductor package org.Hs.eg.db. The three subplots A-C group terms in relation to synaptic function, neuronal development and transportation, respectively.

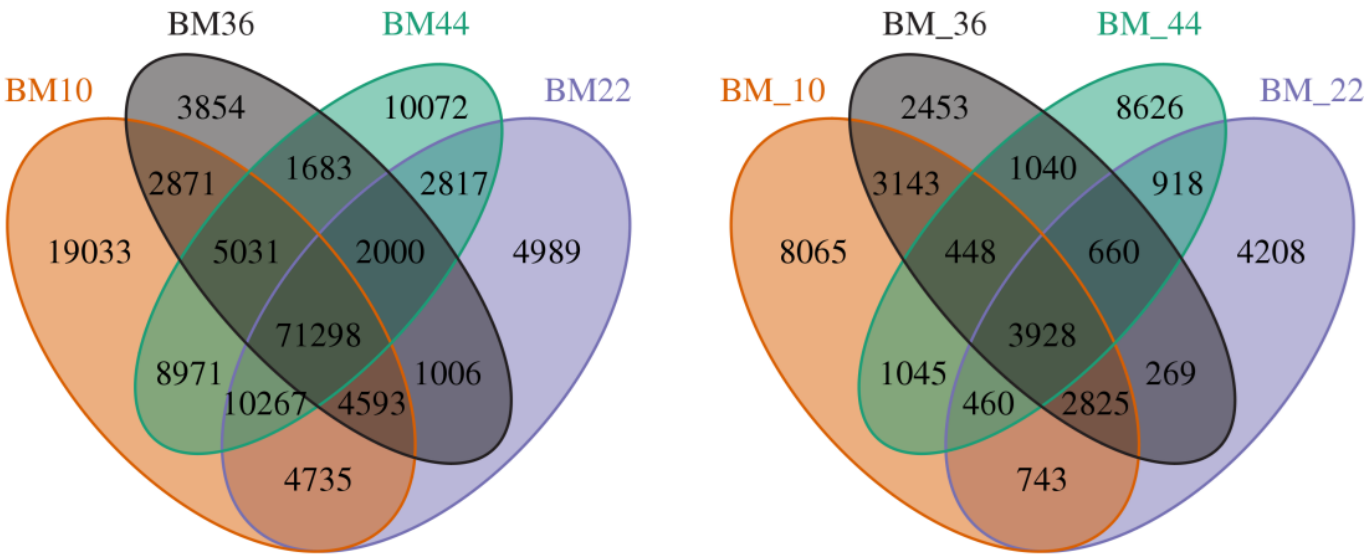

Fig. S7. eQTLs are shared among different regions, related to STAR Methods. Venn-diagram showing the overlap among *cis*-eQTLs (left) and *trans*-eQTLs (right).

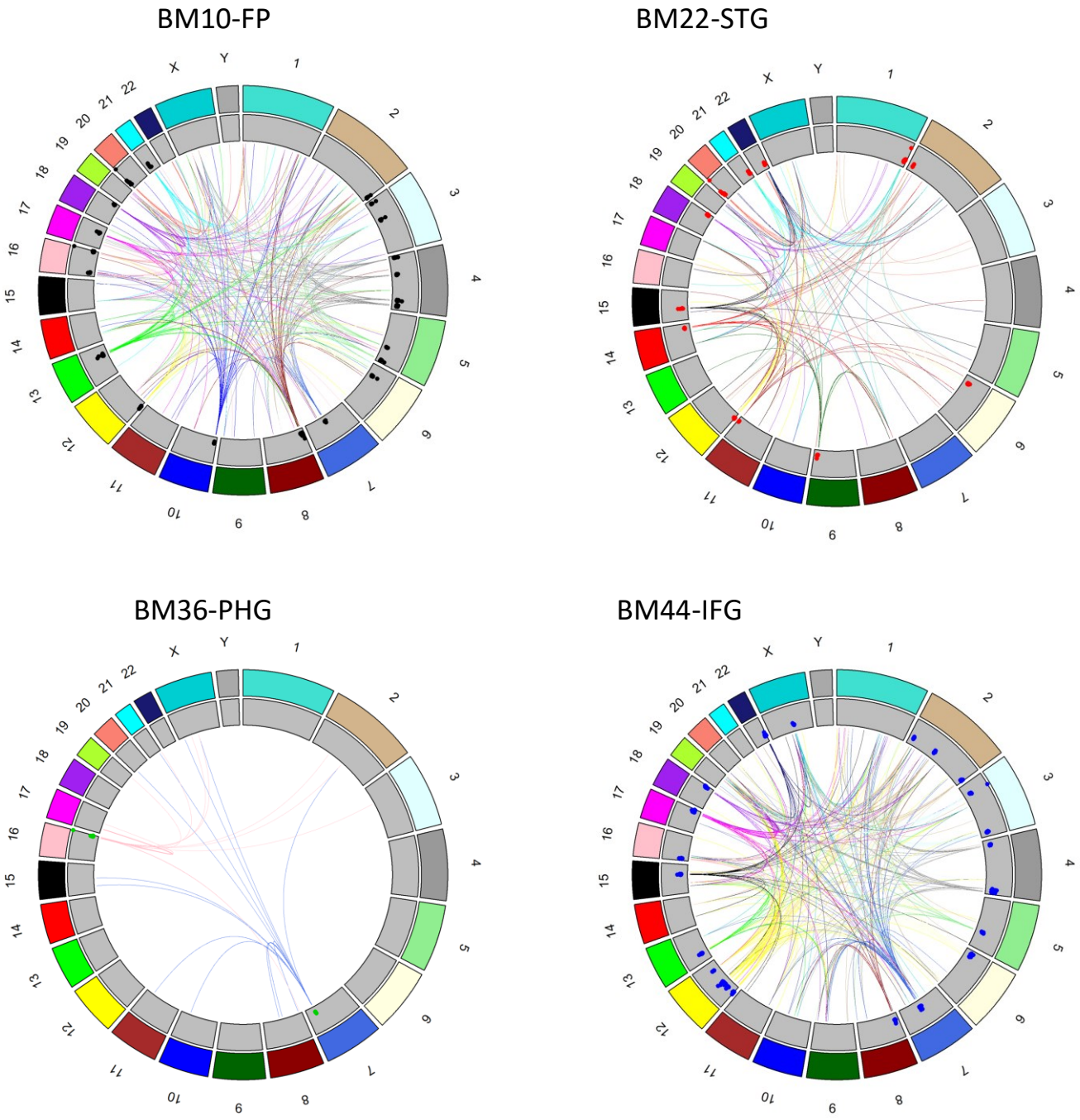

Fig. S8. *Trans*-eQTL hotspots identified in the 4 brain regions, related to STAR Methods. The outermost first track shows the chromosome id. The second track denotes the color coding of the chromosomes. The dots in the third track denote the –log10(P value) of the *trans*-eQTL associations for the hotspots. Links in the middle connect the hotspots to the associated *trans*-eGenes. Links are colored by the chromosomal origination of the *trans*-eQTL hotspots.

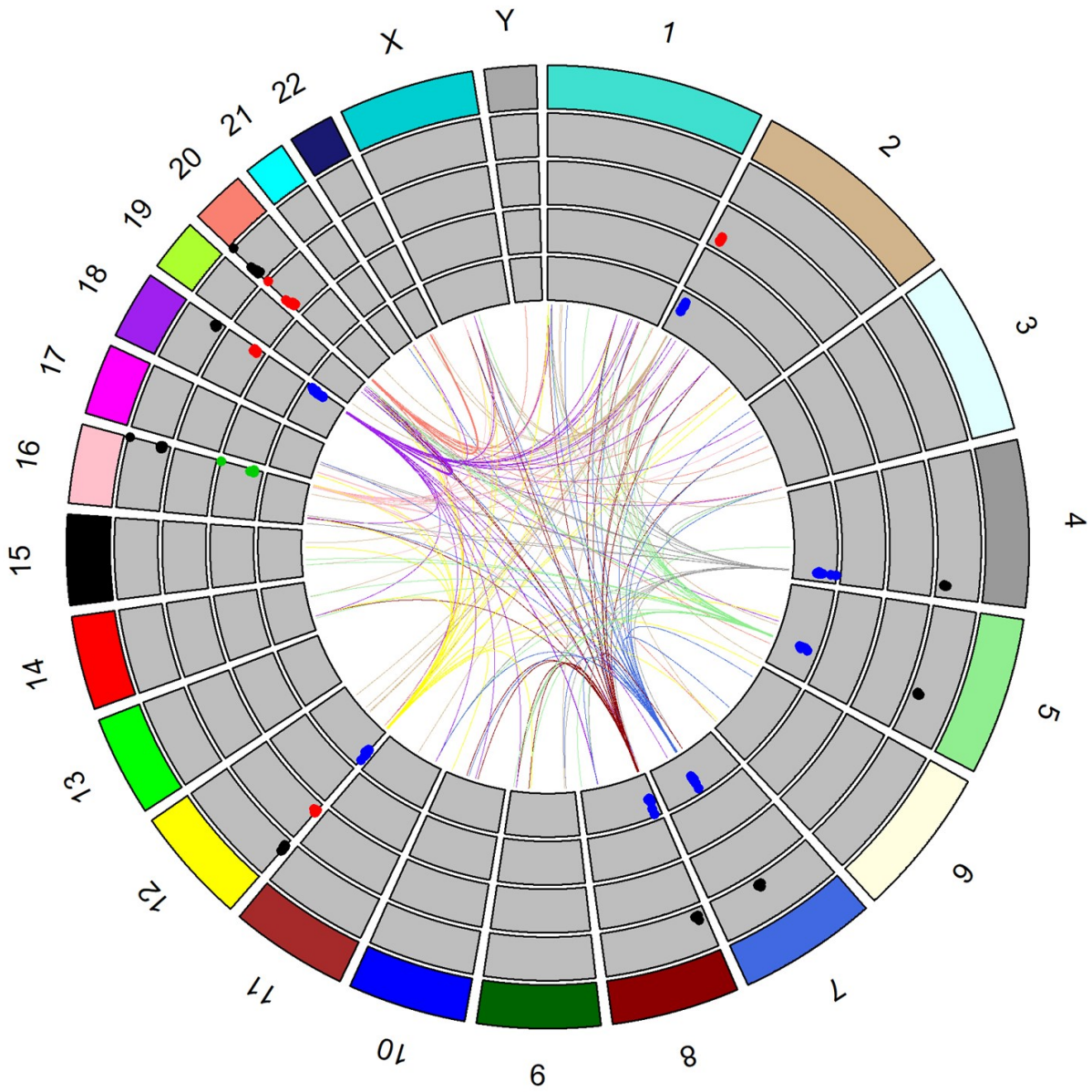

Fig. S9. *Trans*-eQTL hotspots shared by at least two brain regions, related to STAR Methods. The outermost first track shows the chromosome id. The second track denotes the color coding of the chromosomes. The dots in the third to sixth tracks denote the –log10(P value) of the *trans*-eQTL associations for the hotspots in brain region BM10-FP, BM22-STG, BM36-PHG and BM44-IFG, respectively. Links in the middle connect the hotspots to the associated *trans*-eGenes. Links are colored by the chromosomal origination of the *trans*-eQTL hotspots.

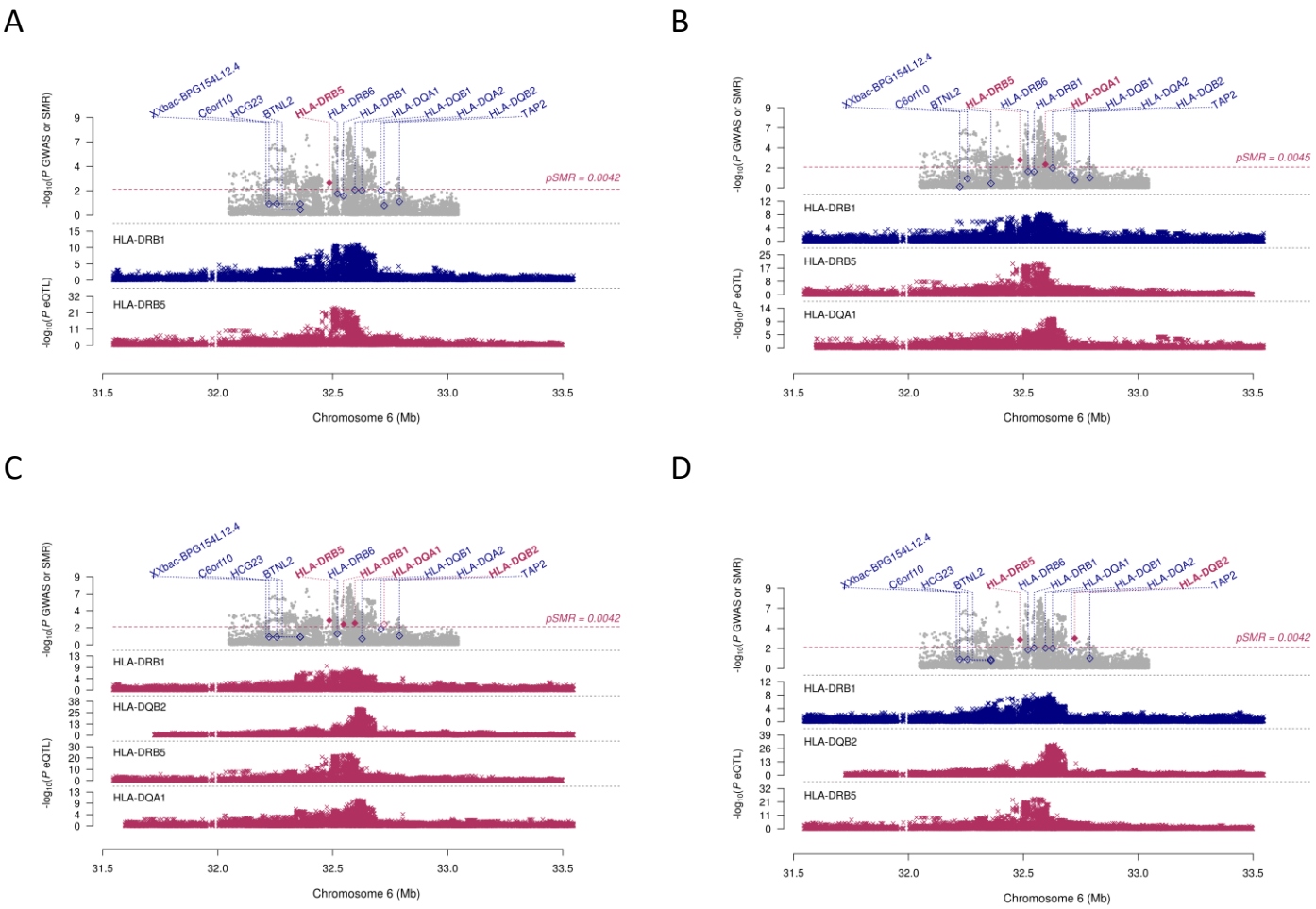

Fig. S10. Summary data-based Mendelian randomization (SMR) analysis at the *HLA-DRB1/HLA-DRB5* locus based on Kunkle et al 2019 AD GWAS summary statistics, related to STAR Methods. A-D show the SMR analysis results integrating IGAP AD GWAS with eQTLs derived from brain regions BM10, BM22, BM36 and BM44, accordingly. For the top panel in each plot, dots represent the P values for SNPs from the IGAP AD GWAS analysis and diamonds represent the P values for genes from the SMR test. Filled diamonds highlight the genes surpassing the HEIDI test ($P \geq 0.05$). The genes with cis-eQTLs are listed on the top. Genes surpassing the SMR test were highlighted in red. Dashed line shows the region-specific Bonferroni corrected P value significance threshold of the SMR test controlling for the number of genes examined. Bottom plot shows the eQTL P values of SNPs from the present data.

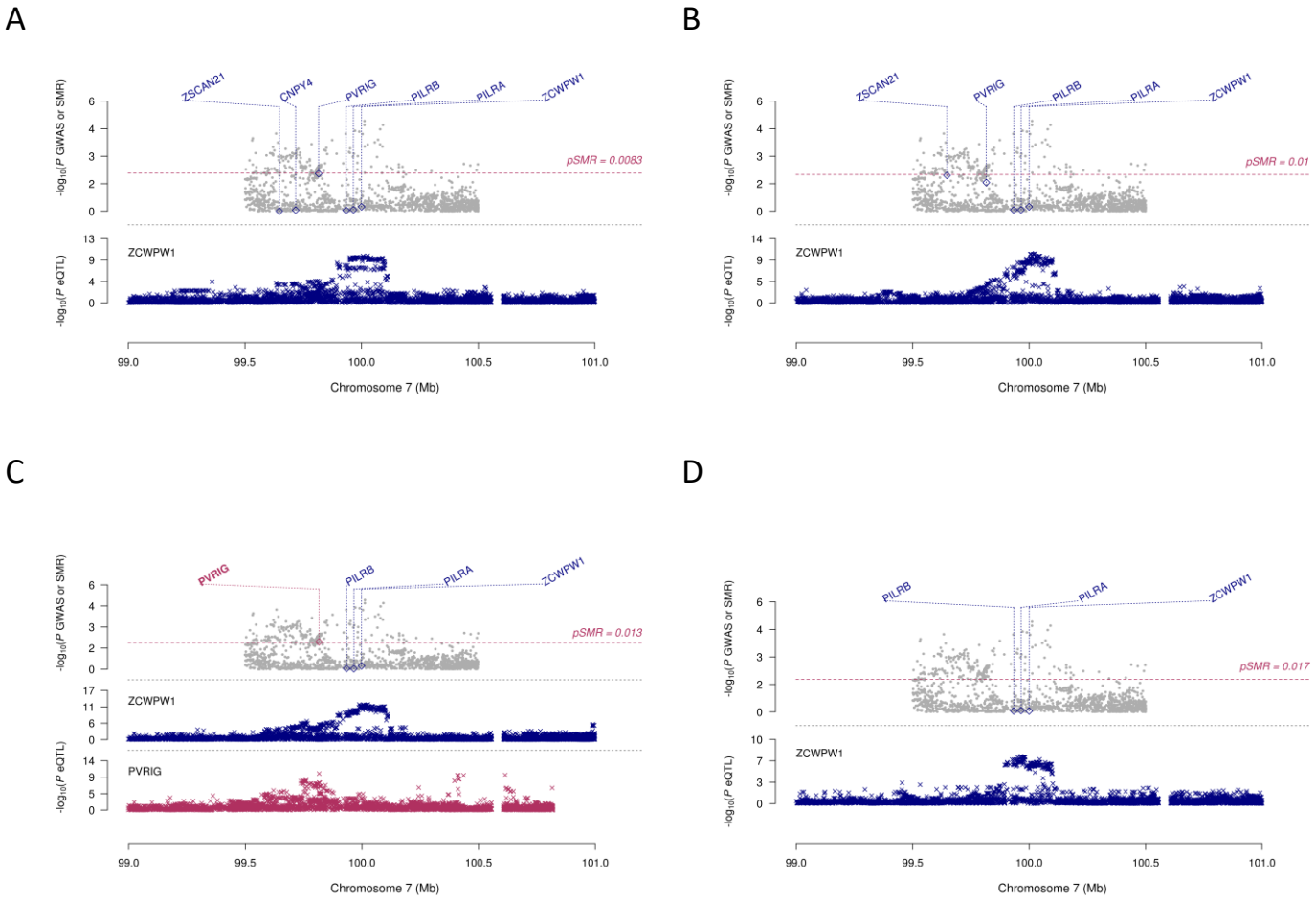

Fig. S11. SMR analysis at the *ZCWPW1* locus based on Kunkle et al 2019 AD GWAS summary statistics, related to STAR Methods. A-D show the results from BM10, BM22, BM36 and BM44, accordingly. Figure legend is the same as in **Fig S11**.

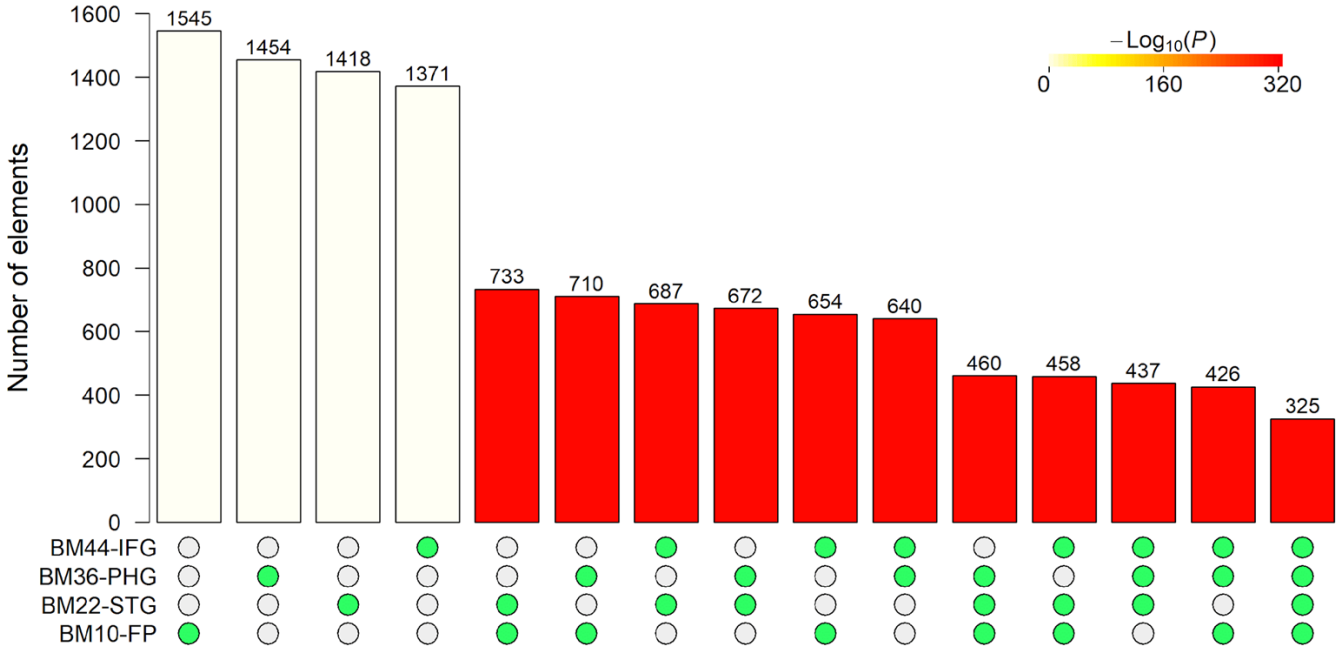

Fig. S12. Bayesian network key drivers are strongly shared among brain region-specific networks, related to STAR Methods. The bar height denotes the number of key drivers overlapping in a given comparison as specified by the green circles underneath. The overlap size is also shown above the bar. The color denotes the P value significance of the overlap size.

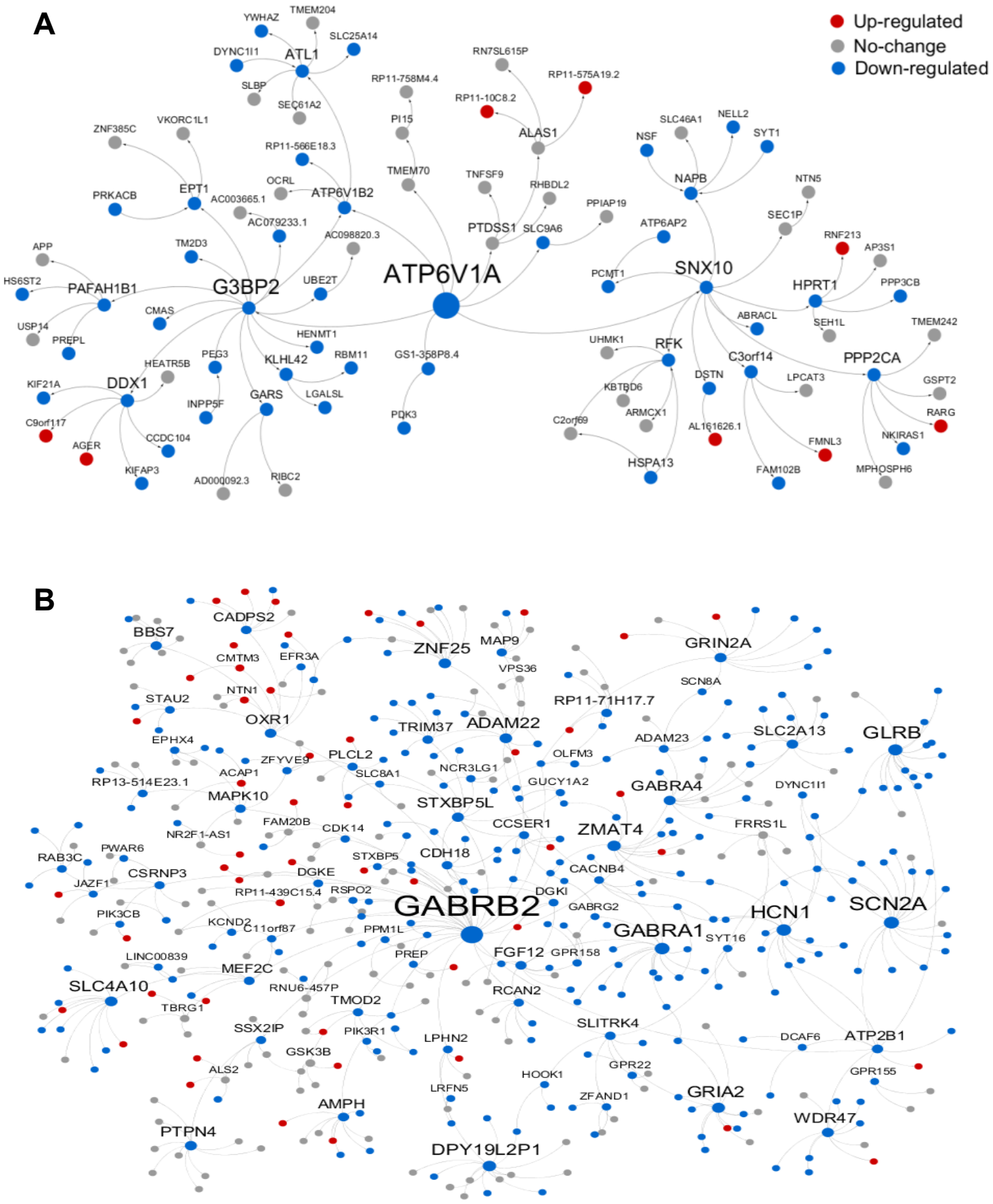

Fig. S13. Network neighborhood of key driver genes *ATP6V1A* and *GABRB2* on the BM36-PHG BN, related to Figure 3 and STAR Methods. Down-regulated genes in demented brains are enriched in network neighboring (A) *ATP6V1A* (FE = 5.4 and FDR = 3.7E-19) and (B) *GABRB2* (FE = 5.8, FDR = 1.1E-106). Node color denotes the direction of gene expression change in in the BM36-PHG region of patients with dementia (CDR ≥ 1).

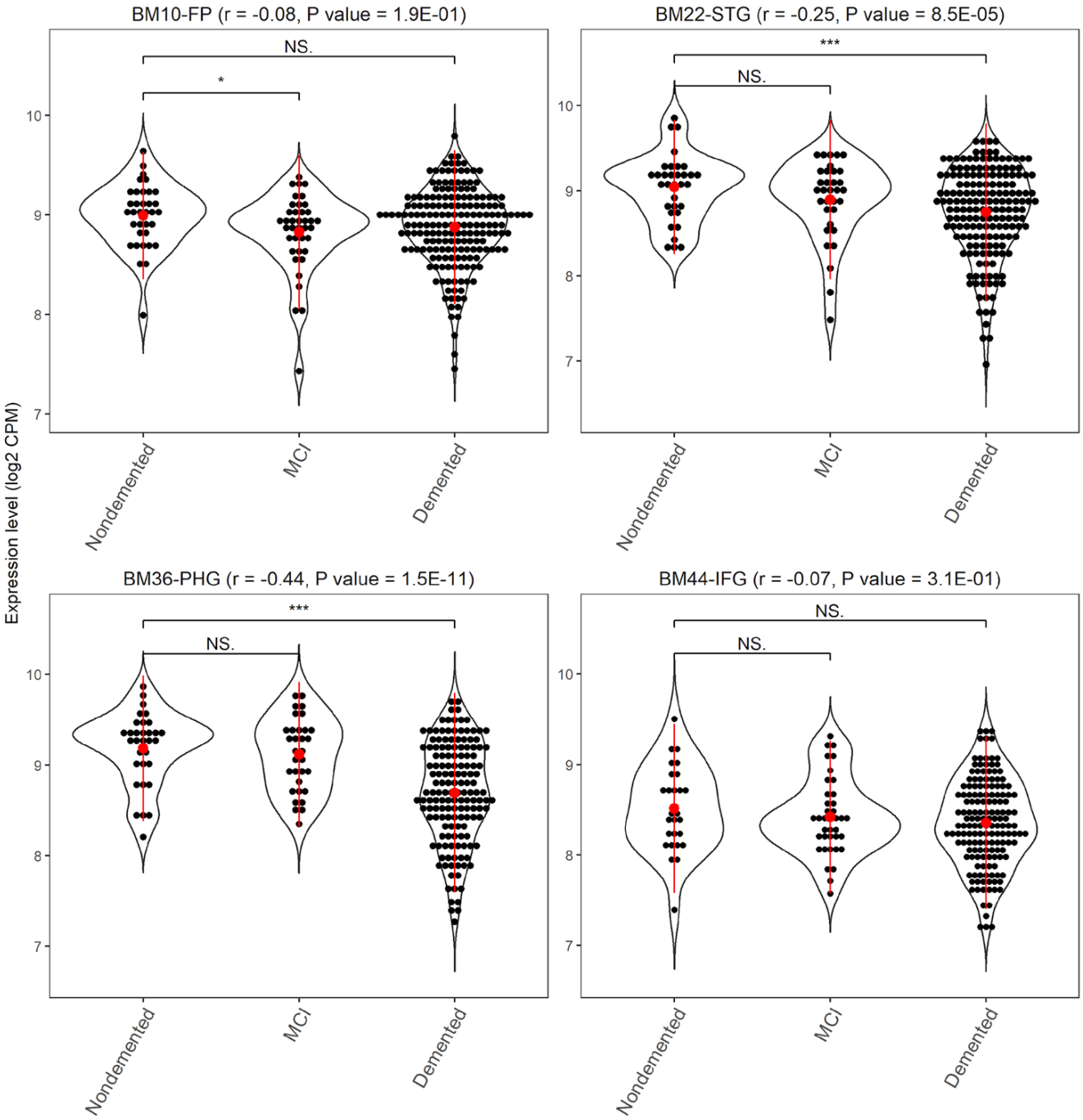

Fig. S14. *ATP6V1A* is down-regulated in demented patients in multiple brain regions, related to Figure 3. Significance bar represents t-test P value. *p < 0.05; ***p < 0.001, NS., no significance. Correlation coefficient (r) and P value of the Spearman correlation between *ATP6V1A* expression and clinical trait CDR are also shown in the top of each sub-plot.

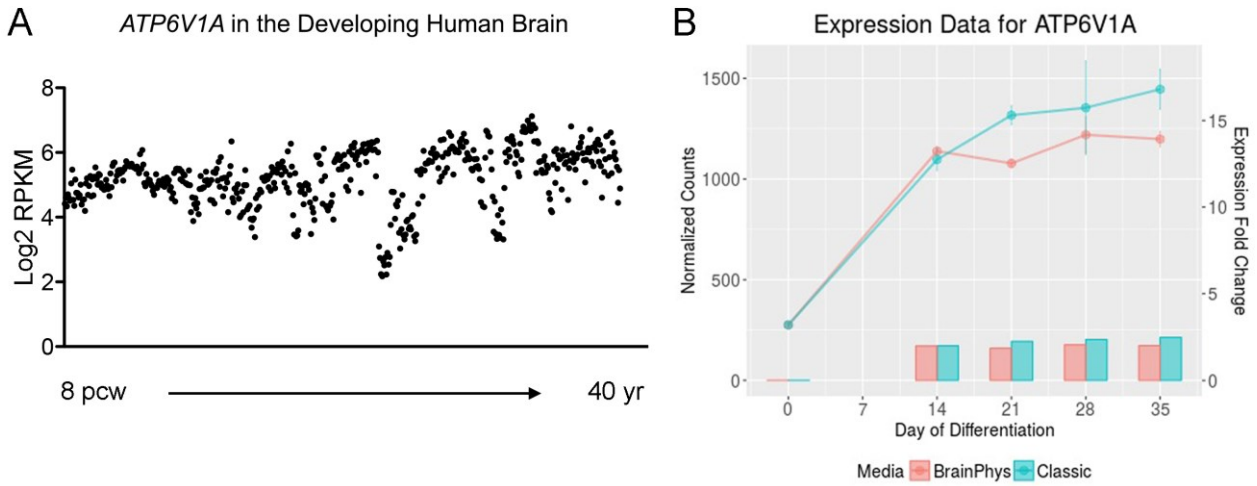

Fig. S15. *ATP6V1A* is robustly expressed among different nerve cells, related to Figure 4. (**A**) A scatter plot represents log2 RPKM (reads per kilobase per million) expression for *ATP6V1A* gene in the developing brain from age 8 pcw to 40 yrs (Miller et al 2014, available from https://www.brainspan.org/rnaseq/search/index.html). (**B**) *ATP6V1A* visualization in human iPSC-derived neurons during *NGN2*-induction (Tian et al. 2019, available from https://ineuronrnaseq.shinyapps.io/rnaseq_app/).

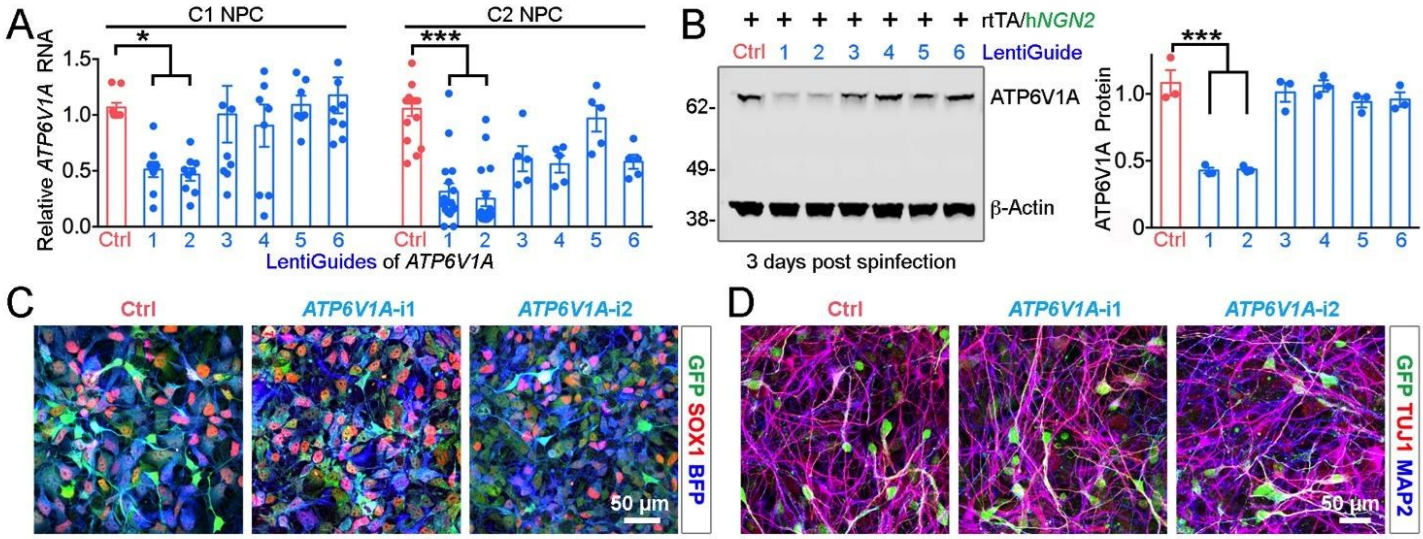

Fig. S16. Evaluation of six gRNAs for repression of *ATP6V1A* in hiPSC-derived NPCs and *NGN2*-neurons, related to Figure 4. A-B, Normalized relative RNA and protein levels (compared to an empty backbone control) following transduction of dCas9-KRAB NPCs with lentivirus-expressing gRNA targeting *ATP6V1A*. Red: control. Blue: CRISPRi. ANOVA; *p < 0.05 and ***p < 0.001; Error bars represent SE. **C-D**, *ATP6V1A* CRISPRi does not affect the neuronal differentiation of NPCs to *NGN2*-neurons. SOX1 is a neural stem cell marker (red); TUJ1 (red) and MAP2 (blue) are pan-neuronal markers. Bars, 50 µm.

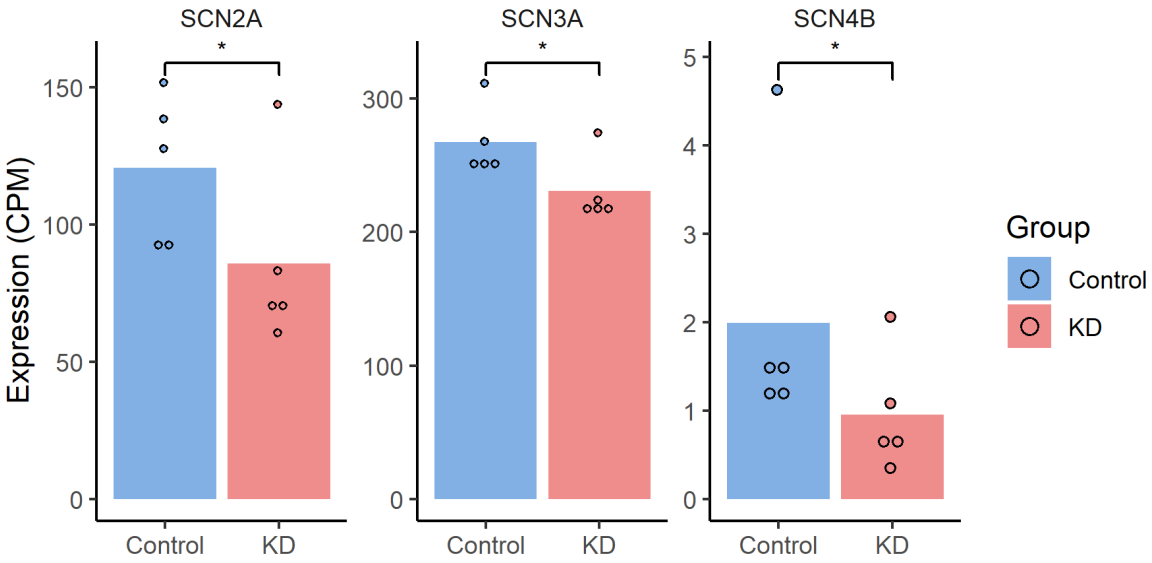

Fig. S17. RNA-seq revealed reduced mRNA expression of voltage gated sodium channel subunits *SCN3A*, *SCN2A*, and *SCN4B* in *ATP6V1A* KD *NGN2*-neurons, related to Figure 4. *p < 0.05 by Student's t-test.

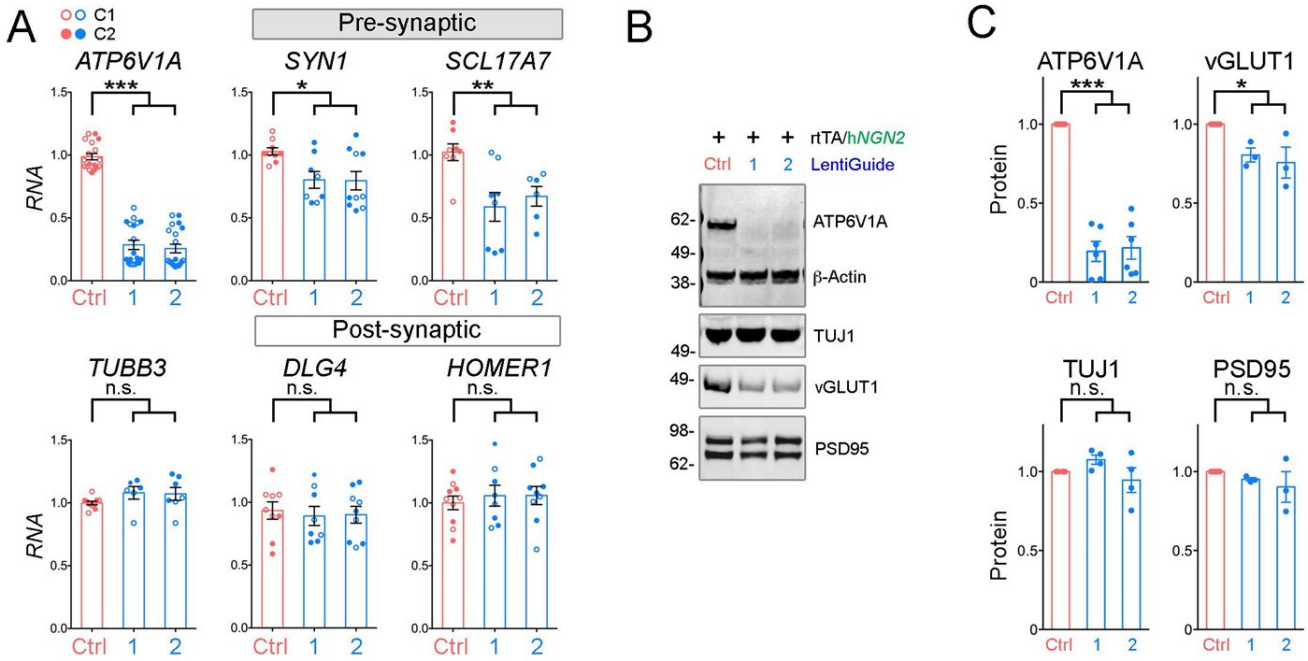

Fig. S18. Expression of synaptic components in hiPSC-derived *NGN2*-neurons, related to Figure 4. A, qRT-PCR analysis of expression of *ATP6V1A*, *TUBB3*, *SYN1*, *SCL17A7*, *DLG4* and *HOMER1* genes. n = 6-20 replicates. **B-C**, Western blot analysis and quantification of ATP6V1A, β-Actin, TUJ1, VGLUT1 and HOMER1 protein levels. Data represent the mean, n = 3 independent experiments. ANOVA; *p < 0.05; **p < 0.01; ***p < 0.001; n.s., no significance; Error bars represent SE.

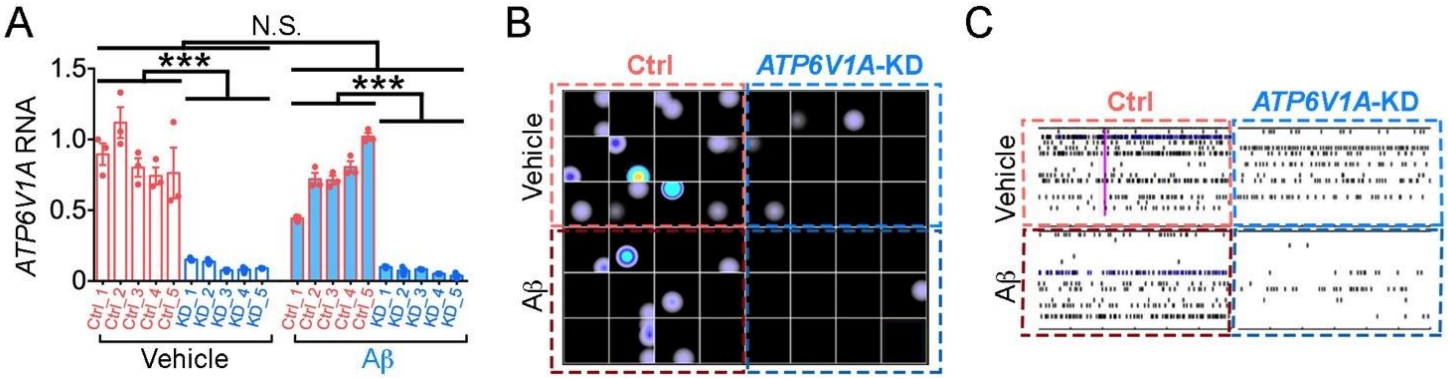

Fig. S19. MEA arrays in *ATP6V1A*-deficient *NGN2*-neurons with or without exposure to Aβ, related to Figure 4. A, *ATP6V1A* RNA levels across different samples. n = 3 replicates. ANOVA; ***p < 0.001; N.S., no significance; Error bars represent SE. **B**, Representative heat map recording of a CytoView MEA 48 plate. **C**, Representative raster plots of the spike events over 10 minutes of day 21 (D21) *NGN2*-neurons.

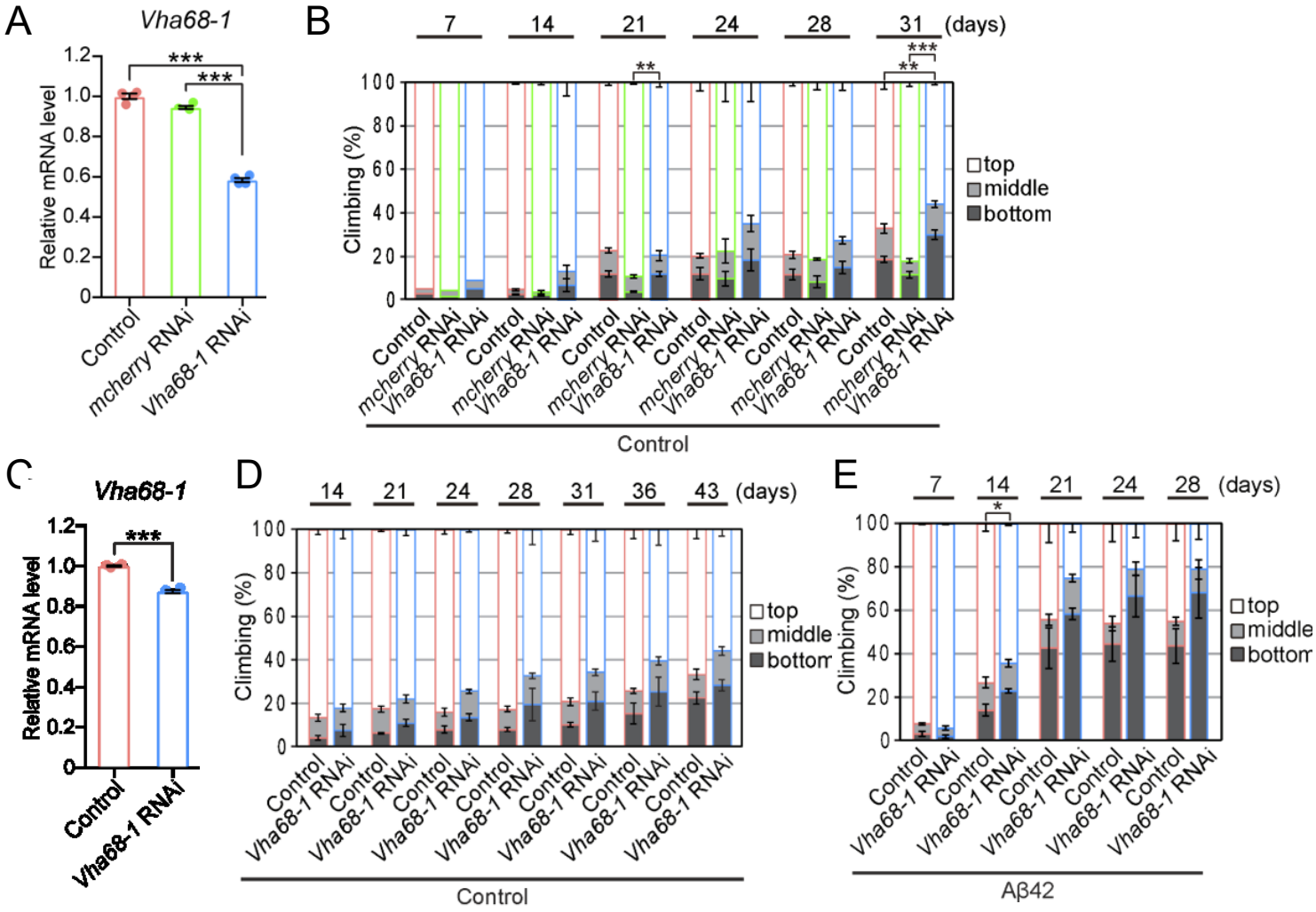

Fig. S20. Neuronal knockdown of *Vha68-1* exacerbates behavioral deficits caused by overexpression of Aβ42 peptide, related to Figure 4. **A**, mRNA expression levels of *Vha68-1* in heads of flies expressing RNAi targeting *Vha68-1* (line #50726) were analyzed by qRT-PCR. n = 4, ***p < 0.001 by Student's t-test. **B**, Neuronal knockdown of *Vha68-1* (line #50726) by itself caused modest decline in climbing ability in aged flies. Average percentages of flies that climbed to the top (white), climbed to the middle (light gray), or stayed at the bottom (dark gray) of the vials. Percentages of flies that stayed at the bottom were subjected to statistical analyses. n = 5 independent experiments except for day 7 when n = 2, **p < 0.01 and ***p < 0.001 by Student's t-test. **C**, mRNA levels of *Vha68-1* in heads of flies expressing RNAi targeting *Vha68-1* (line #42888) were analyzed by qRT-PCR. n = 4, ***p < 0.001 by Student's t-test. **D-E**, Neuronal knockdown of *Vha68-1* (line #42888) did not alter climbing ability in control flies (**D**) but slightly enhanced locomotor deficits in Aβ42 flies (**E**). Percentages of flies that stayed at the bottom were subjected to statistical analyses. n = 5 independent experiments, **p < 0.01 and ***p < 0.001 by Student's t-test. The genotypes of the flies were: **A** and **B**, (Control): *elav*-GAL4/Y; +/CyO, (*mcherry* RNAi): *elav*-GAL4/Y; +/CyO; UAS-*mcherry* RNAi/+, (*Vha68-1* RNAi): *elav*-GAL4/Y; +/CyO; UAS-*Vha68-1* RNAi (line #50726)/+. **C** and **E**, (Control): *elav*-GAL4/Y, (*Vha68-1* RNAi): *elav*-GAL4/Y; UAS-*Vha68-1* RNAi (line #42888)/+. **D**, (Aβ42 and Control): *elav*-GAL4/Y; UAS-Aβ42/+; and (Aβ42 and *Vha68-1* RNAi): elav-GAL4/Y; UAS-Aβ42/UAS-*Vha68-1* RNAi (line #42888).

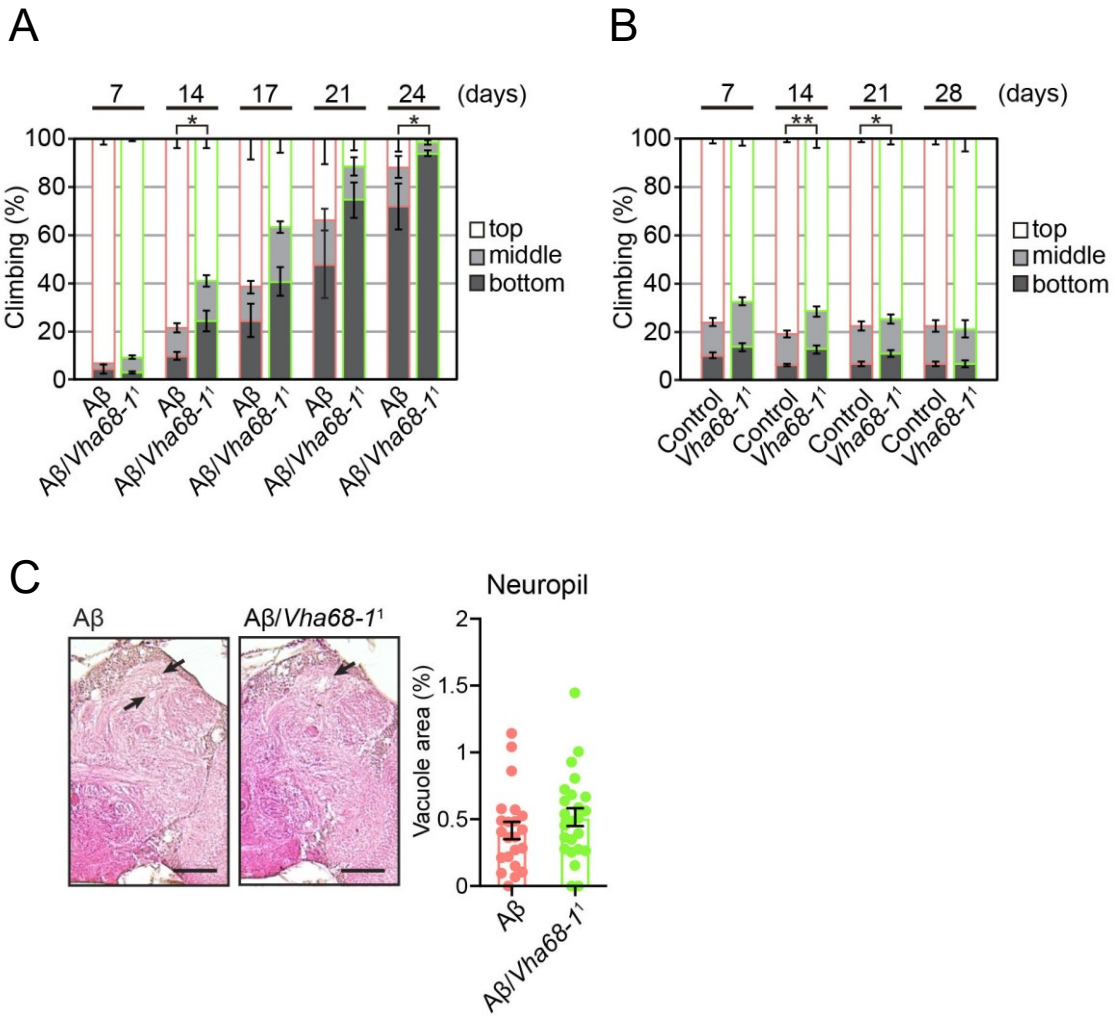

Fig. S21 A single nucleotide mutation of *Vha68-1* worsens Aβ42-induced climbing defects, related to Figure 4. (**A**) A heterozygous mutation of *Vha68-1*^{1} worsened locomotor defects caused by Aβ42 as revealed by climbing assay. (**B**) A heterozygous mutation of *Vha68-1*^{1} by itself did not cause obvious climbing defects. Percentages of flies that stayed at the bottom were subjected to statistical analyses. n = 3-4 independent experiments. $^{*}p < 0.05$ and $^{**}p < 0.01$ by Student's *t*-test. (**C**) A heterozygous mutation of *Vha68-1*^{1} slightly worsened neurodegeneration in the neuropil region in Aβ42 fly brains, but the difference did not reach statistical significance. Representative images show the central neuropil in the paraffin-embedded brain section with hematoxylin and eosin (HE) staining from 24-day-old flies. Scale bars: 50 μm. Percentages of vacuole areas (indicated by arrows in the images) were subjected to statistical analyses. n = 22-24 hemispheres. The genotypes of the flies were (Aβ): *elav*-GAL4/Y;UAS-Aβ42/+, (Aβ/*Vha68-1*^{1}): *elav*-GAL4/Y;UAS-Aβ42/*Vha68-1*^{1}. (Control): *elav*-GAL4/Y and (*Vha68-1*^{1}): *elav*-GAL4/Y; *Vha68-1*^{1}/+.

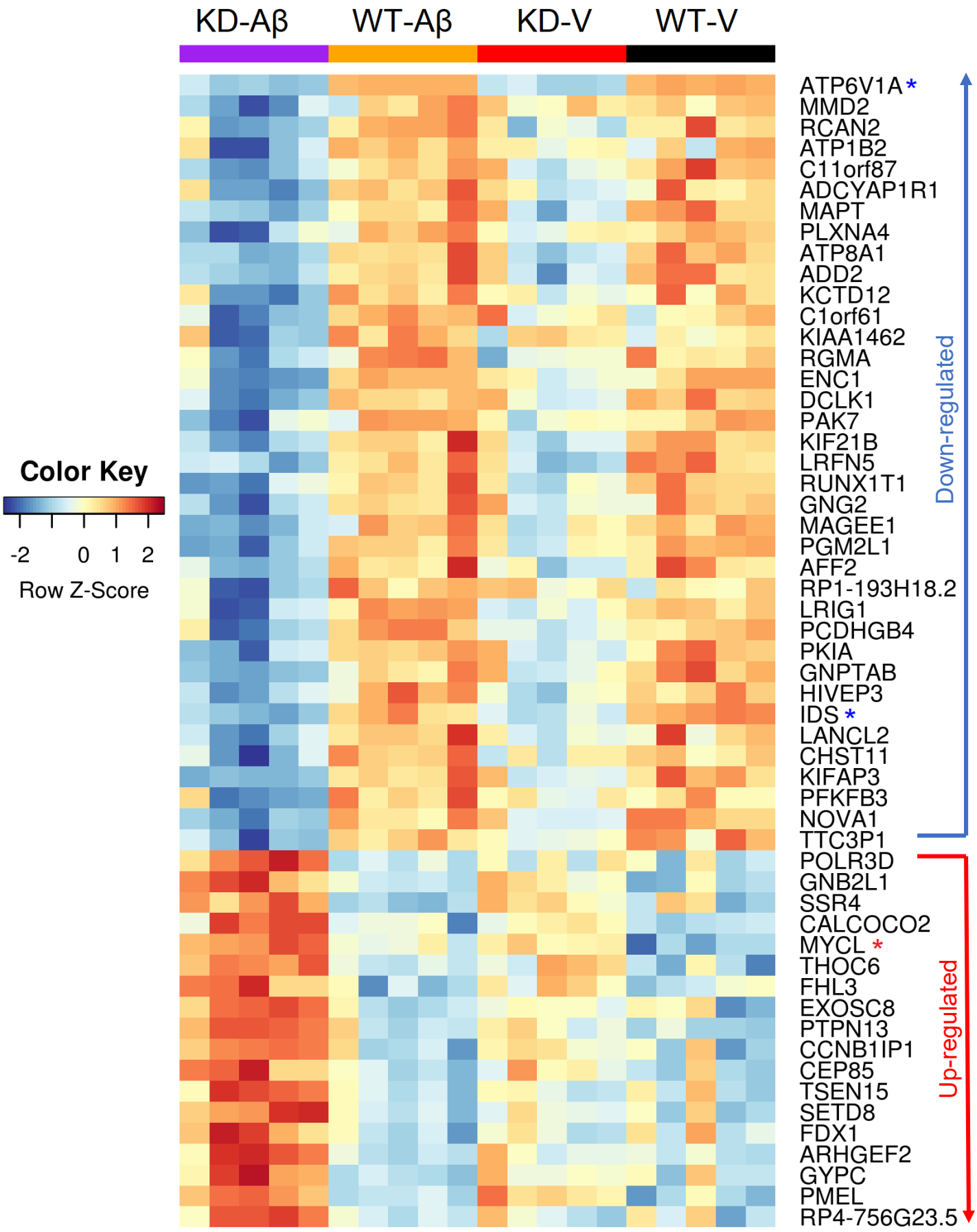

Fig. S22. Heat-map showing genes significantly differentially expressed between *ATP6V1A* KD and WT in *NGN2*-neurons with or without Aβ treatment, related to Figure 5. The expression values have been converted to z-score. Blue and red asterisks (*) denote, respectively, the genes consistently down- or up-regulated irrespective of Aβ treatment (i.e. KD-V vs WT-V and KD-Aβ vs WT-Aβ). Genes without any symbol annotation are detected only in Aβ treated cells (i.e. KD-Aβ vs WT-Aβ).

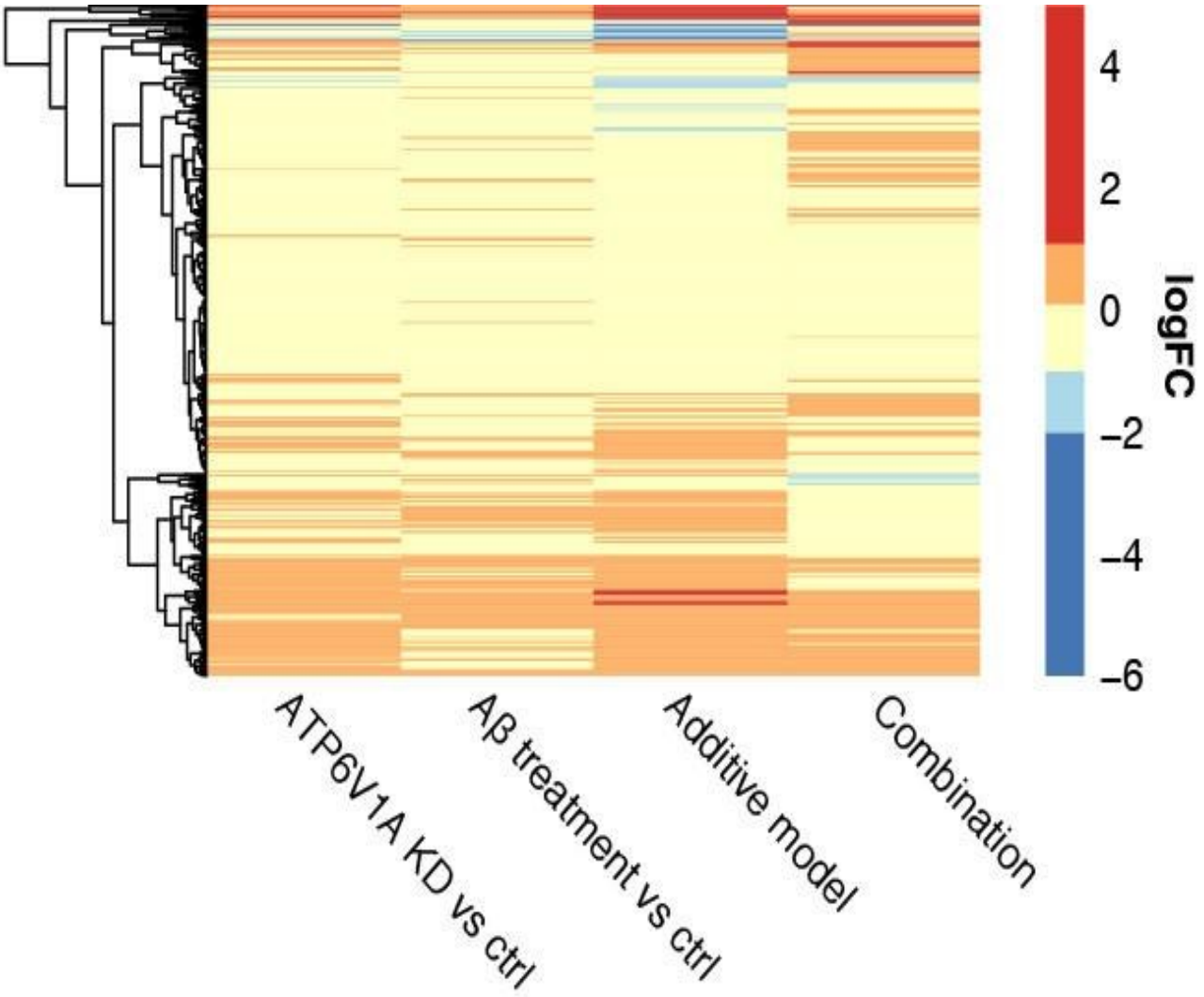

Fig. S23. Hierarchical clustering of differential expression log2 fold changes (logFC) for all contrasts in *NGN2*-neurons treated with *ATP6V1A* KD and/or Aβ, related to Figure 5. Genes were pre-aggregated using k-means (k=500). Color gradient represents logFC.

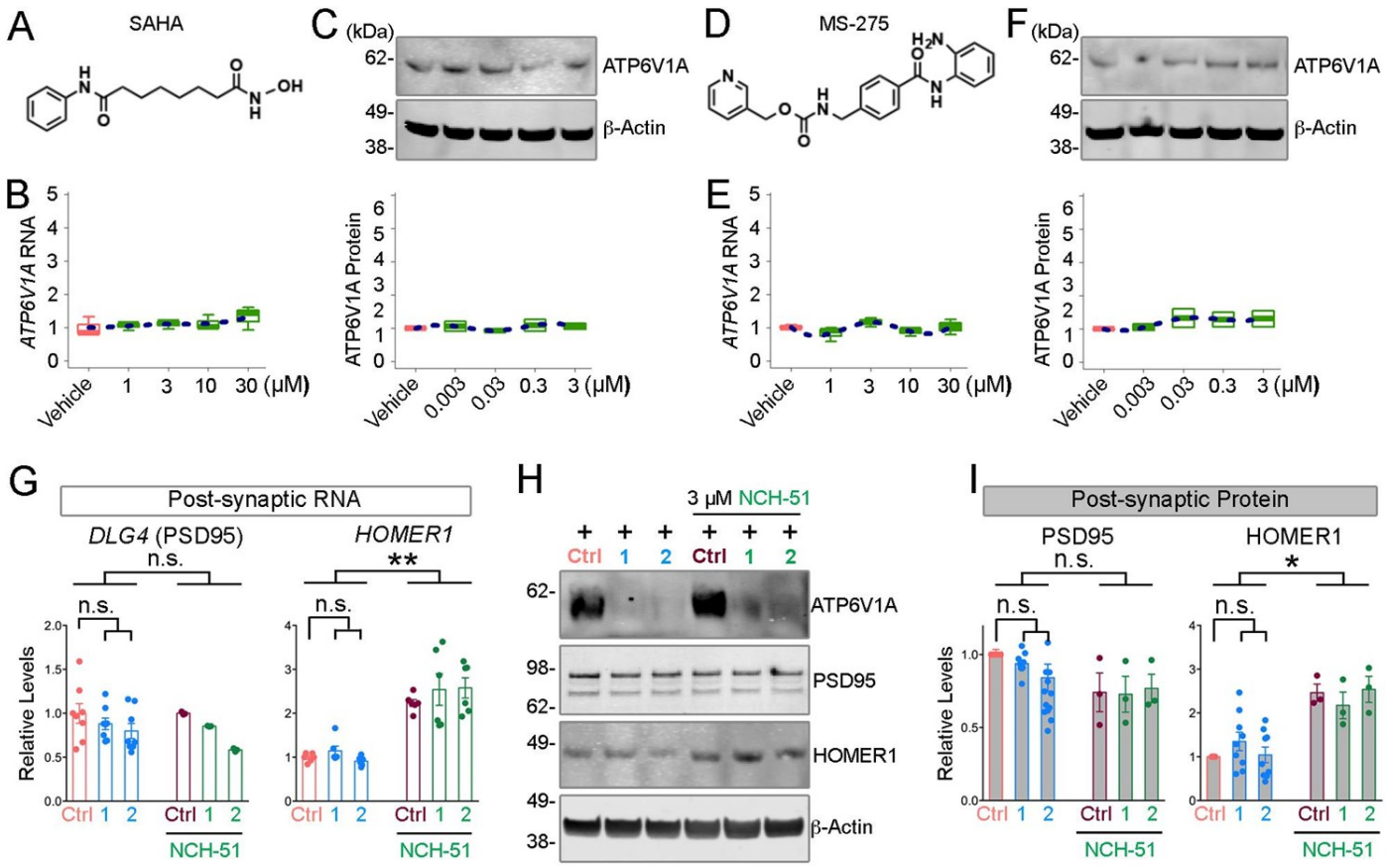

Fig. S24. Effects of SAHA and MS-275 on *ATP6V1A* mRNA level and NCH-51 on postsynaptic expression in *NGN2*-neurons, related to Figure 6. A-F, HDAC inhibitors SAHA and MS-275 have no effect on ATP6V1A levels. Chemical structures of SAHA (**A**) and MS-275 (**D**). Effects of SAHA (**B**) and MS-275 (**E**) at 1, 3, 10, 30 μM on *ATP6V1A* mRNA levels 24-h after exposure. Effects of SAHA (**C**) and MS-275 (**F**) at 0.003, 0.03, 0.3, 3 μM on ATP6V1A protein level 48-h after exposure, analyzed by western blot. β-Actin is a loading control. A blue dotted line is curve fitted for the set of data points. **G**, qRT-PCR analysis of *ATP6V1A* and the postsynaptic *PSD95* and *HOMER1* mRNA expression in *NGN2*-neurons in the absence and presence of 3 μM NCH-51. n = 3-8 replicates. **H-I**, Representative western blot and quantitative analysis (n = 3-10 replicates) of ATP6V1A, PSD95 and HOMER1 protein. β-Actin is a loading control. ANOVA; *p < 0.05; **p < 0.01; ***p < 0.001; n.s., no significance; Error bars represent SE.

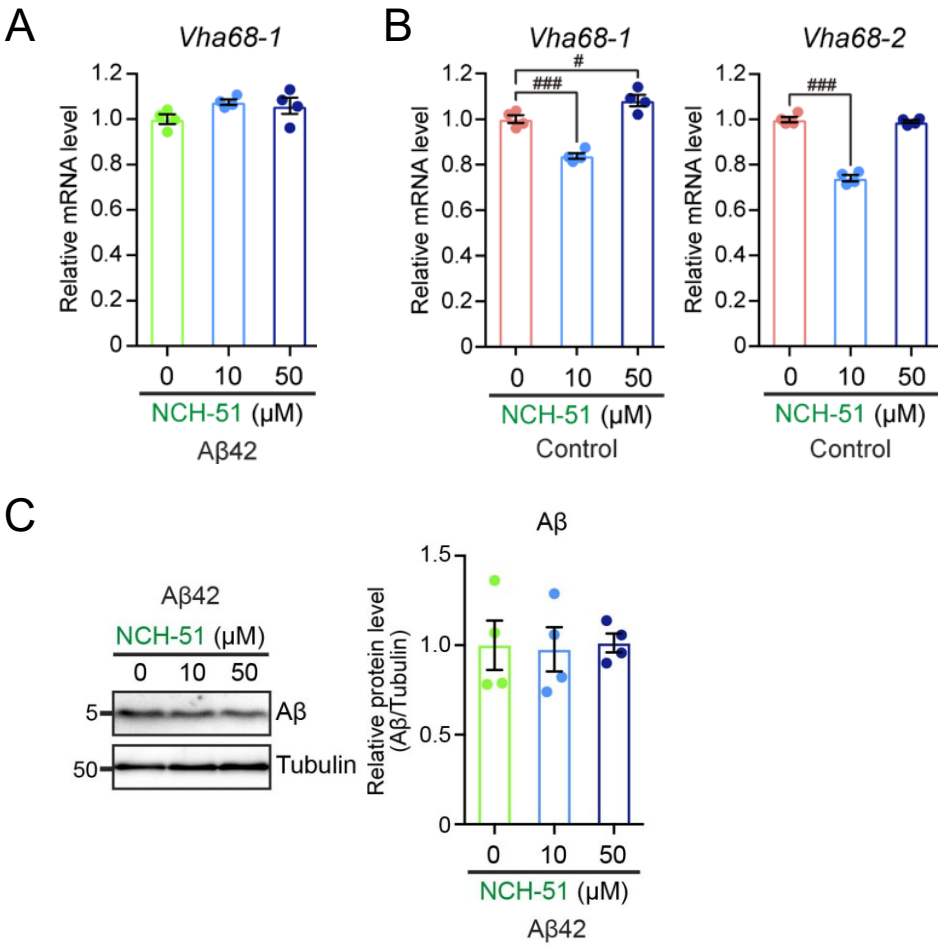

Fig. S25. A novel compound, NCH-51 suppresses neurodegeneration in Aβ42 flies, related to Figure 6. A, Administration of NCH-51 did not increase mRNA levels of *Vha68-1* in Aβ42 flies. **B**, mRNA levels of *Vha68-1* and *Vha68-2* in control flies fed with NCH-51 were analyzed by qRT-PCR. n = 4, #p < 0.05, ###p < 0.001 by one-way ANOVA with Dunnett's post hoc test. **C**, Administration of NCH-51 did not affect Aβ42 levels in fly brains. Aβ42 peptides from fly heads were analyzed by western blotting with anti-Aβ antibody. n = 4. The genotypes of the flies were (Aβ42): *elav*-GAL4/Y; UAS-Aβ42 /+ and (Control): *elav*-GAL4/Y.

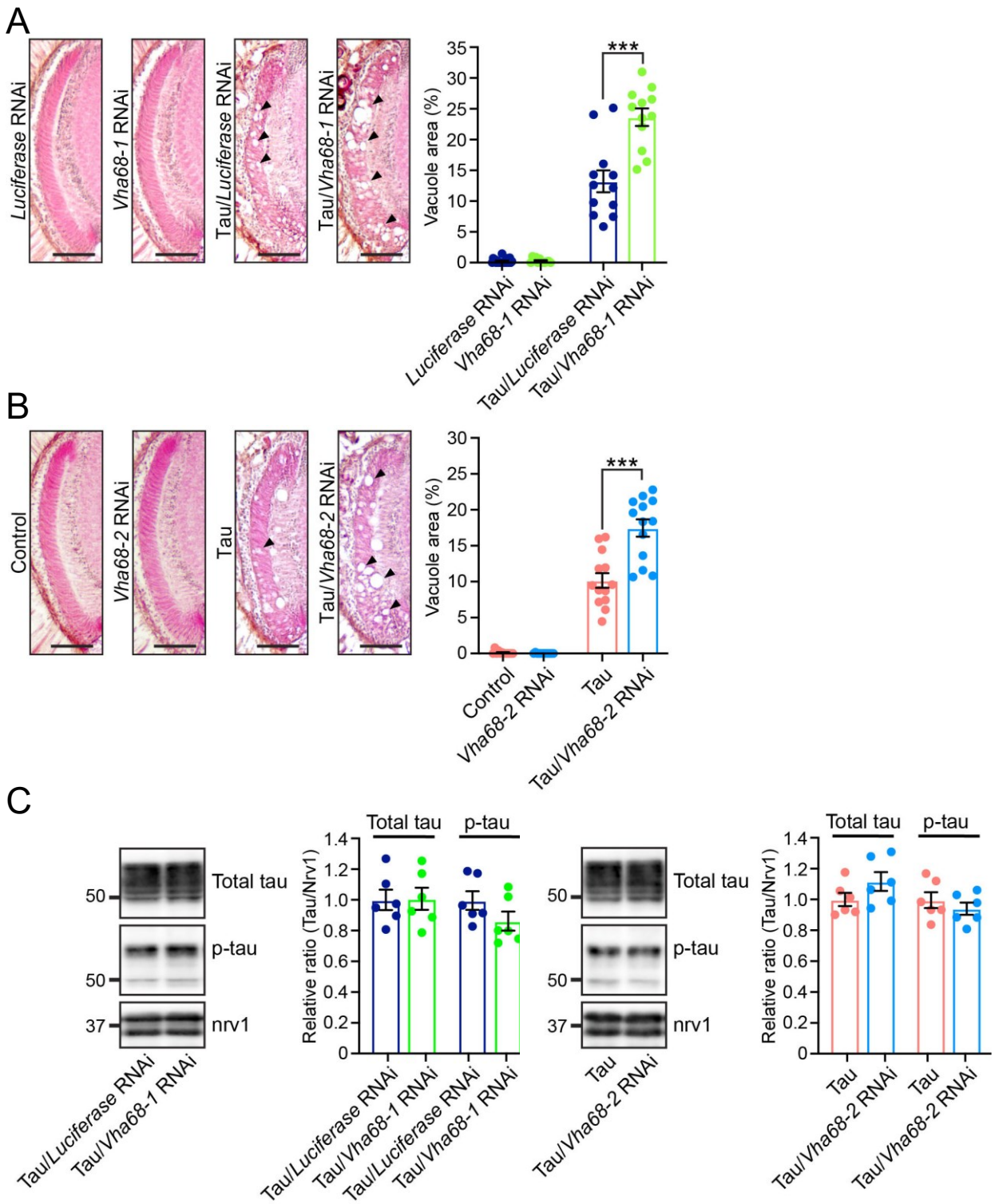

Fig. S26. Knockdown of *Vha68-1* or *Vha68-2* exacerbates axon degeneration caused by overexpression of human tau, related to STAR Methods. Knockdown of *Vha68-1* (**A**) or *Vha68-2* (**B**) in fly eyes exacerbated axon degeneration in the lamina caused by ectopic overexpression of human tau. Representative images show the lamina in paraffin-embedded head section with hematoxylin and eosin (HE) staining from 7-day-old flies. Scale bars: 50 μm. Percentages of vacuole areas in the lamina (indicated by arrowheads in the images) are shown. n = 12 hemispheres, $^{***}p < 0.001$ by Student's t-test. (**C**) Knockdown of *Vha68-1* or *Vha68-2* did not alter either the total or phosphorylation levels of tau. Fly heads expressing tau alone (Tau) or co-expressing tau and RNAi targeting for *Vha68-1* or *Vha68-2* subjected to western blotting with anti-tau or anti-phospho tau (AT8, pS202/T205) antibodies. Nervana (nrv1), a fly ortholog of ATPase Na^+/K^+ transporting subunit β 1, was used as the loading control. n = 6. The genotypes of the flies were (*Luciferase* RNAi): +/Y; *GMR*-GAL4/UAS-*Luciferase* RNAi, (*Vha68-1* RNAi): +/Y; *GMR*-GAL4/UAS-*Vha68-1* RNAi, (Tau/*Luciferase* RNAi): +/Y; *GMR*-GAL4, UAS-tau/*Luciferase* RNAi, (Tau/*Vha68-1* RNAi): +/Y; *GMR*-GAL4, UAS-tau/UAS-*Vha68-1* RNAi, (Control): +/Y; *GMR*-GAL4/+, (*Vha68-2* RNAi): +/Y; *GMR*-GAL4/+; UAS-*Vha68-2* RNAi/+, (Tau); +/Y; *GMR*-GAL4, UAS-tau/+ and (Tau/*Vha68-2* RNAi): +/Y; *GMR*-GAL4, UAS-tau/+; UAS-*Vha68-2* RNAi/+.

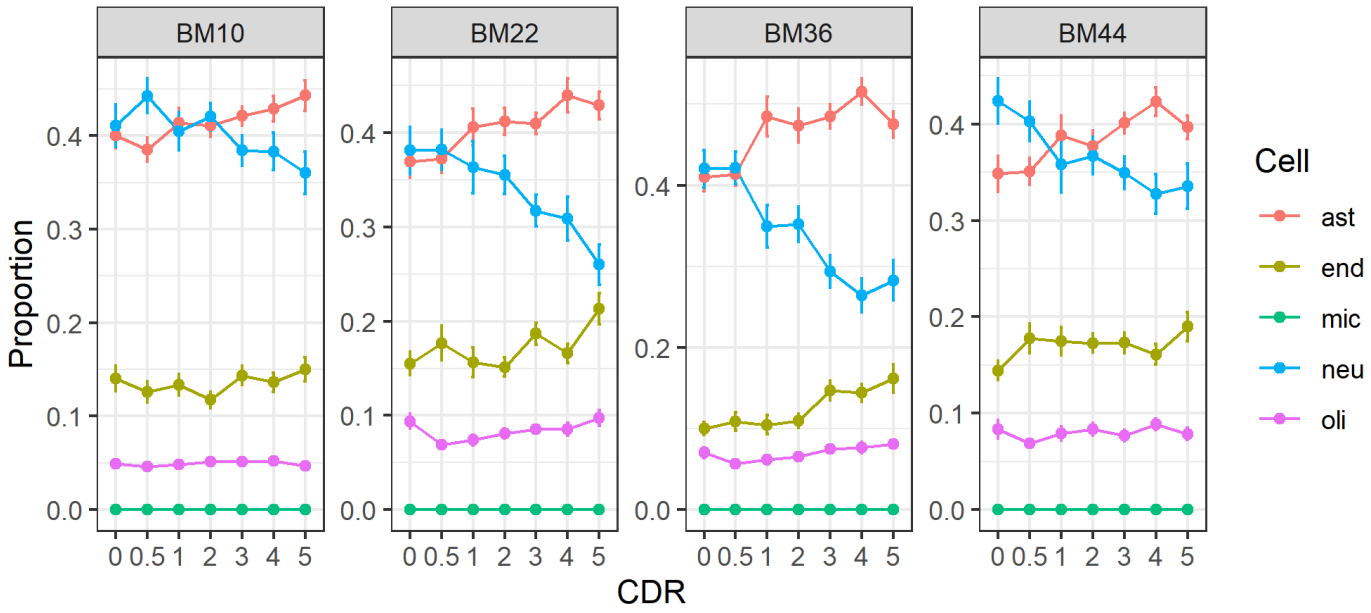

Fig. S27. Distribution of cell type frequency estimates stratified by CDR, related to STAR Methods. Error bar denotes standard error. Ast, astrocyte; end, endothelial; mic, microglia; neu, neurons; oli, oligodendrocytes. The proportion of microglia cells was not estimable, likely due to the low sensitivity in estimating cells with low abundance.